Disentangling the Influences of Storm-Relative Flow and Horizontal Streamwise Vorticity on Low-Level Mesocyclones in Supercells

JOHN M. PETERS,[a] BRICE E. COFFER,[b] MATTHEW D. PARKER,[b] CHRISTOPHER J. NOWOTARSKI,[c]
JAKE P. MULHOLLAND,[e] CAMERON J. NIXON,[d] AND JOHN T. ALLEN[d]

[a] *Department of Meteorology and Atmospheric Science, The Pennsylvania State University, University Park, Pennsylvania*
[b] *Department of Marine, Earth and Atmospheric Sciences, North Carolina State University, Raleigh, North Carolina*
[c] *Department of Atmospheric Sciences, Texas A&M University, College Station, Texas*
[d] *Department of Earth and Atmospheric Sciences, Central Michigan University, Mount Pleasant, Michigan*
[e] *Department of Atmospheric Sciences, University of North Dakota, Grand Forks, North Dakota*

(Manuscript received 18 May 2022, in final form 11 September 2022)

ABSTRACT: Sufficient low-level storm-relative flow is a necessary ingredient for sustained supercell thunderstorms and is connected to supercell updraft width. Assuming a supercell exists, the role of low-level storm-relative flow in regulating supercells' low-level mesocyclone intensity is less clear. One possibility considered in this article is that storm-relative flow controls mesocyclone and tornado width via its modulation of overall updraft extent. This hypothesis relies on a previously postulated positive correspondence between updraft width, mesocyclone width, and tornado width. An alternative hypothesis is that mesocyclone characteristics are primarily regulated by horizontal streamwise vorticity irrespective of storm-relative flow. A matrix of supercell simulations was analyzed to address the aforementioned hypotheses, wherein horizontal streamwise vorticity and storm-relative flow were independently varied. Among these simulations, mesocyclone width and intensity were strongly correlated with horizontal streamwise vorticity, and comparatively weakly correlated with storm-relative flow, supporting the second hypothesis. Accompanying theory and trajectory analysis offers the physical explanation that, when storm-relative flow is large and updrafts are wide, vertically tilted streamwise vorticity is projected over a wider area but with a lesser average magnitude than when these parameters are small. These factors partially offset one another, degrading the correspondence of storm-relative flow with updraft circulation and rotational velocity, which are the mesocyclone attributes most closely tied to tornadoes. These results refute the previously purported connections between updraft width, mesocyclone width, and tornado width, and emphasize horizontal streamwise vorticity as the primary control on low-level mesocyclones in sustained supercells.

SIGNIFICANCE STATEMENT: The intensity of a supercell thunderstorm's low-level rotation, known as the "mesocyclone," is thought to influence tornado likelihood. Mesocyclone intensity depends on many environmental attributes that are often correlated with one another and difficult to disentangle. This study used a large body of numerical simulations to investigate the influence of the speed of low-level air entering a supercell (storm-relative flow), the horizontal spin of the ambient air entering the thunderstorm (streamwise vorticity), and the width of the storm's updraft. Our results suggest that the rotation of the mesocyclone in supercells is primarily influenced by streamwise vorticity, with comparatively weaker connections to storm-relative flow and updraft width. These findings provide important clarification in our scientific understanding of how a storm's environment influences the rate of rotation of its mesocyclone, and the associated tornado threat.

KEYWORDS: Deep convection; Wind shear; Mesocyclones; Severe storms; Supercells; Tornadoes

1. Introduction

Essential to the understanding and prediction of supercell tornadoes is a fundamental understanding of the processes that regulate their parent low-level mesocyclone.[1] This is because the pressure perturbations within supercell mesocyclones result in strong near-surface vertical accelerations (e.g., Rotunno and Klemp 1985), which vertically stretch near-ground vertical vorticity contributing to tornadogenesis (e.g., Doswell and Burgess 1993; Wicker and Wilhelmson 1995; Dowell and Bluestein 2002; Skinner et al. 2014; Markowski and Richardson 2014; Davies-Jones 2015; Markowski and Richardson 2017; Murdzek et al. 2020) and tornado maintenance (e.g., Wicker and Wilhelmson 1995). Consequently, there is evidence that mesocyclone intensity influences tornado likelihood (Coffer and Parker 2015; Coffer et al. 2017; Coffer and Parker 2018), size (Trapp et al. 2017), and wind speeds (Marion et al. 2019; Sessa and Trapp 2020), so long as the other necessary ingredients for tornadogenesis are present. These other necessary ingredients include vertical vorticity at the surface (Doswell and Burgess 1993), an optimal outflow buoyancy (Markowski et al. 2002; Brown and Nowotarski 2019), and vertical alignment between near-surface vertical vorticity and the mesocyclone (Guarriello et al. 2018). Because of the strong influence of mesocyclone characteristics on tornadogenesis, a large body of research over the last half century has sought to better understand the

---

[1] In this article, "low level" will refer to the mesocyclone near cloud base. For the remainder of this paper, "low-level mesocyclones" will simply be referred to as "mesocyclones."

Corresponding author: John M. Peters, john.m.peters@psu.edu

DOI: 10.1175/JAS-D-22-0114.1

connections between the characteristics of a storm's environmental wind profile and the storm's mesocyclone size and rotation. Our intent in the present article is to clarify these connections.

The importance of environmental horizontal vorticity in the formation of mesocyclones was first recognized in Browning and Landry (1963) and Barnes (1970). Beginning with Davies-Jones (1984), a series of seminal theoretical studies (Davies-Jones 2008, 2017, 2022) have shown that horizontal streamwise vorticity, which is the component of the vorticity pointed in the direction of the storm-relative wind, is necessarily present within a storm's inflow for the updraft to attain net positive vertical vorticity, and consequently cohesive updraft rotation. In turn, strong net updraft rotation at low levels within a supercell results in stronger near-ground vertical accelerations and a greater chance of increasing near-ground rotation to tornadic intensity (Wicker and Wilhelmson 1995; Markowski and Richardson 2014; Coffer and Parker 2015; Coffer et al. 2017). In addition to environmentally derived horizontal vorticity, storm-generated horizontal vorticity within supercell cold pools is also an important source of streamwise vorticity to low-level mesocyclones (Rotunno and Klemp 1985; Davies-Jones and Brooks 1993; Dahl et al. 2014; Davies-Jones 2022). Hence, the strong influence of both environmentally derived and storm-generated horizontal streamwise vorticity on mesocyclone characteristics is well established in past literature.

Storm-relative helicity (SRH), which is a popular supercell and tornado forecast parameter, is the vertically integrated product of horizontal streamwise vorticity and storm-relative wind (Lilly 1986; Davies-Jones et al. 1990; Droegemeier et al. 1993; Brooks et al. 1993). The use of SRH in research and forecasting of supercells and tornadoes has become prevalent during the last several decades in both the United States (e.g., Thompson et al. 2003, 2007, 2012; Coffer et al. 2019) and Europe (e.g., Coffer et al. 2020; Taszarek et al. 2020). This quantity is generally larger in tornadic supercell environments than in their nontornadic counterparts (Markowski et al. 2003; Parker 2014; Coniglio and Parker 2020). All else being equal, a supercell is thought to have a more intense mesocyclone when environmental SRH is large, relative to when environmental SRH is small. This idea is consistent with past theoretical analyses that have related the covariance of vertical vorticity and vertical velocity in updrafts to the environmental SRH (e.g., Davies-Jones 1984, 2022). Consequently, tornadogenesis is considered more probable when SRH is large in a supercell's environment because of the connections between a mesocyclone and near-ground stretching of vertical vorticity.

Because the formula for SRH contains the vertically integrated storm-relative flow magnitude multiplied by horizontal streamwise vorticity, the use of SRH in forecasting supercell mesocyclones and tornadoes implicitly introduces the layer-integrated (or proportionally, layer-averaged) storm-relative flow magnitude as a predictor of these storm attributes. *This leads us to question whether storm-relative flow itself exerts a direct influence on mesocyclone intensity and tornadoes*. There is ample evidence connecting layer-averaged storm-relative flow to the general characteristics of supercell updrafts, such as overall updraft width and maximum updraft vertical velocities (Droegemeier et al. 1993; Warren et al. 2017; Peters et al. 2019, 2020b,c,d, 2022a,b). Indeed, both Droegemeier et al. (1993) and Peters et al. (2020d) found that a lower bound of low-level layer-averaged storm-relative flow of roughly 10 m s^{-1} was necessary for a sustained supercell to exist in their simulations, which implies that a lower bound of this quantity is necessary for supercell tornadoes to occur (e.g., Parker and Dahl 2015). This "critical lower threshold" is likely a consequence of sufficiently strong low-level storm-relative flow ensuring that outflow does not "undercut" the updraft (e.g., Klemp and Wilhelmson 1978; Brooks et al. 1994; Brown and Nowotarski 2019), and that an updraft need-be sufficiently wide to overcome the deleterious effects of entrainment-driven dilution and attain a steady state (Peters et al. 2020c; Morrison et al. 2020; Peters et al. 2020a, 2022a,b).

Assuming that there is sufficient low-level layer-averaged storm-relative flow and other supportive environmental conditions for a supercell to exist, there is inconclusive evidence for a link between storm-to-storm variations in the low-level layer-averaged storm-relative flow magnitude and mesocyclone and tornado behavior. For instance, studies of storm proximity soundings from the Rapid Update Cycle (RUC) show minimal differences in low-level storm-relative wind magnitude between tornadic and nontornadic supercells (e.g., Thompson 1998). In fact, both Markowski et al. (2003) and Nowotarski and Jensen (2013) showed evidence that ground-relative flow is a more skillful discriminator of tornadic from nontornadic supercells than storm-relative flow, which possibly relates to the relationship between ground-relative flow and the frictional generation of near-surface horizontal vorticity (e.g., Flournoy and Rasmussen 2021; Fischer and Dahl 2022). In contrast, an analysis of field project radiosonde launches by Coniglio and Parker (2020) found that low-level storm-relative flow was statistically larger in tornadic than in nontornadic supercells, though the degree to which local storm-driven accelerations were responsible for these trends is unclear. Further exacerbating the uncertainty, the magnitude of storm-relative flow appears in the denominator of equations for updraft vertical vorticity [e.g., Eq. (12) in Klemp 1987], *which implies an inverse relationship between the vertical vorticity in mesocyclones and storm-relative flow*.

It has also been suggested that wide supercell updrafts tend to produce wider and more intense mesocyclones and tornadoes (Trapp et al. 2017; Marion and Trapp 2019; Marion et al. 2019; Sessa and Trapp 2020) than their narrower counterparts. If true, this link supports a possible connection between the low-level layer-averaged storm-relative flow magnitude and mesocyclone intensity, implying that storm-relative flow regulates mesocyclone intensity via its connection with updraft width. For instance, Trapp et al. (2017) showed that progressively increasing the low-level hodograph length in idealized supercell simulations resulted in progressively wider and more intense updrafts and mesocyclones. However, Trapp et al. (2017) varied the low-level storm-relative flow and low-level horizontal streamwise vorticity magnitudes simultaneously in their simulations. Since updraft width is strongly connected to storm-relative flow and mesocyclone intensity is strongly connected to horizontal streamwise vorticity, it is possible that the connection between updraft width and mesocyclone width in these studies was simply an artifact of their experiment design. Furthermore, the physical explanation for this connection between mesocyclones and tornadoes provided by Trapp et al. (2017), which assumes that the rapid rotation in tornadoes originates from the radial contraction of angular momentum in the tornado's parent mesocyclone, has been debated (Coffer and Markowski 2018). It is generally understood that air parcels in tornadoes originate in convective outflow and a storm's environmental inflow (e.g., Dahl et al. 2014; Fischer and Dahl 2022), rather than from within the tornado's parent updraft. Hence, the existence of this possible connection between storm-relative flow, updraft width, and supercell mesocyclones is unclear.

Given the aforementioned scientific questions, the objective of the present article is to clarify the role of storm-relative flow in supercell mesocyclones. We consider the following opposing hypotheses:

- H1: Low-level layer-averaged storm-relative flow and environmental[2] horizontal streamwise vorticity together (with comparable influence) regulate the mesocyclone size and intensity via their combined regulation of the mesocyclone width and the vertical vorticity magnitude.
- H2: Assuming there is sufficient low-level layer-averaged storm-relative flow for a sustained supercell to exist, mesocyclone size and rotation are primarily regulated by the environmental horizontal streamwise vorticity magnitude.

We address these hypotheses with a matrix of idealized large-eddy simulations (LESs) of supercell thunderstorms, which are introduced in section 2 and analyzed in section 3. We provide theoretical support for our conclusions in section 4. Our results are summarized and discussed in section 5.

2. Simulations

a. Model configuration

Our experiment consisted of a matrix of 32 LESs of supercells simulated within environments with independently varied low-level horizontal streamwise vorticity and low-level storm-relative flow (and by extension updraft radius). This setup is designed to address our hypotheses by allowing us to investigate the separate influences of these environmental characteristics on mesocyclones. Our simulations used Cloud Model 1 (CM1) version 20.3 (Bryan and Fritsch 2002) with a time-splitting acoustic integration scheme (psolver = 2 in the namelist.input file). Model dimensions were 400 km with 1152 grid points in the horizontal directions, and 25 km with 250 grid points in the vertical direction. We also used horizontal and vertical "grid stretching" options (stretch_x = 1, stretch_y = 1, stretch_z = 2 in the namelist.input file). The horizontal grid spacing was 100 m within the inner 100-km-wide square positioned at the domain center, and increased outward from this inner fine mesh to 4056 m at the domain boundaries. The vertical grid spacing was uniform at 25 m below 2000 m, and then gradually increased to 250 m by the domain top. These stretching options achieved an LES resolution within the regions of the domain that contained active convective updrafts, while maintaining a coarser resolution in less vital domain regions, such as in the stratosphere and near the domain boundaries far from convective updrafts. We also used an adaptive time step (adapt_dt = 1 in the namelist.input file) with an initial time step of 0.5 s. Subgrid-scale turbulence was parameterized using the Smagorinsky option in CM1 with separate horizontal and vertical turbulence coefficients (sgsmodel = 2 with tconfig = 2 in the namelist.input file), and microphysics were parameterized with the double-moment scheme of Morrison et al. (2009) with hail as the prognostic rimed ice species. All other simulation attributes that are not explicitly discussed below were set to their default values in the namelist.input file of the CM1 version 20.3 release.

Lateral domain boundaries were set to the open radiative option (Durran and Klemp 1983), and the top boundary was set to free slip. The lower boundary was set to the semislip option with a surface drag coefficient of 1.4×10^{-2}, and with other attributes consistent with Coffer and Parker (2017). Following Coffer and Parker (2017), a Coriolis force of $f = 10^{-4}\ \mathrm{s}^{-1}$ was applied, and was balanced by a fictitious large-scale pressure gradient force (icor = 1 and lspgrad = 1 in the namelist.input file). This is an identical configuration to what was referred to as "Coriolis applied to the perturbation wind only" in the older release of CM1 used in Coffer et al. (2017). We also used the "spinup" method of Coffer and Parker (2017), wherein CM1 was run as a single-column model until the vertical wind profile had reached a quasi-steady state, after roughly 15 h. The resulting "spun-up" vertical wind profiles were used as initial conditions for our supercell simulations.

We initiated convection using the "updraft nudging" technique of Naylor and Gilmore (2012), with the nudging region located at the domain center with a horizontal radius of 10 km, a vertical center point of 1500 m AGL, a vertical radius of 1500 m, an e-folding time of 0.5 s^{-1}, a maximum vertical velocity w value of 10 m s^{-1}, and a gradual ramp down of the nudging amplitude between the simulation times of 15 and 20 min. Domainwide random potential temperature θ perturbations with a maximum amplitude of 0.25 K were also included in the initial conditions to facilitate the development of turbulence. To minimize the potential influence of the updraft nudging on our results, we did not analyze any simulation times until 20 min after the nudging had ceased. Spurious vertical vorticity from updraft nudging that exists for longer than 20 min is possible (e.g., Fischer and Dahl 2022), but is unlikely to change the interpretation of our results given our focus on low-level mesocyclones, rather than the initial stages of tornadogenesis. Total integration times in all simulations were 3 h. Finally, we used a trial-and-error method to adjust the domain translation velocity so that the right-moving storms were approximately centered in the model domain in each simulation.

---

[2] While this study focuses on how a storm's surrounding environment influences its mesocyclone, we recognize the potentially important influence of storm-generated (baroclinic) vorticity on low-level mesocyclones, and plan to study this influence in the future.

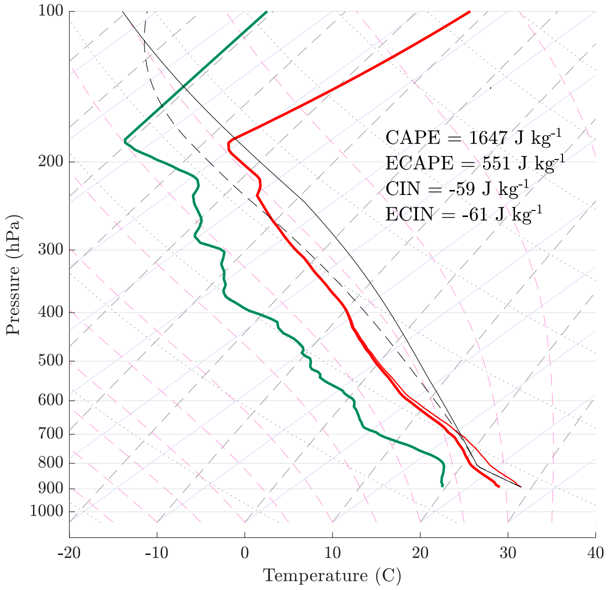

FIG. 1. Skew $T-\log p$ diagram of the VORTEX2 composite tornadic supercell sounding from Parker (2014). The environmental T (K), density temperature T_ρ (K), and dewpoint temperature T_d (K) are shown in thick red, thin red, and thick green, respectively. Black lines are the T_ρ for undiluted (solid) and entraining (dashed; fractional entrainment rate $\varepsilon = 1 \times 10^{-4}$ m^{-1}) parcels lifted adiabatically from the surface using the method of Peters et al. (2022c). Density temperature is defined following Peters et al. (2022c) as $T_\rho \equiv T[1 + (R_d/R_v)q_v - q_t]$, where T is the temperature of the lifted parcel, R_d and R_v are the dry-air and water vapor specific gas constants (set to their values in CM1), q_v is the water vapor mass fraction of the lifted parcel (specific humidity), and q_t is the total water mass fraction of the lifted parcel. Convective available potential energy (CAPE) and convective inhibition (CIN) for the undiluted parcel (CAPE and CIN, respectively), and for the entraining parcel (ECAPE and ECIN, respectively) are listed in the upper-right corner.

b. Model vertical temperature and wind profiles

All of our simulations use the composite vertical thermodynamic profile of observed soundings near tornadic supercells in the Verification of the Origins of Rotation in Tornadoes Experiment 2 (VORTEX2; Wurman et al. 2012) that was generated in Parker (2014) (see Fig. 1). Our simulations were run with two different general hodograph shapes. The first shape followed the "L-shaped profile" of Chavas and Dawson (2021) (denoted in the simulation name with an "L," Fig. 2), wherein the shear is purely in the y direction below a critical height h, and then switches to being purely in the x direction above h. The formula for this profile is

$$\begin{aligned} u(z) &= u_b, \\ v(z) &= v_b + s_1 z, \end{aligned} \tag{1}$$

below height h, where u_b and v_b are constants, and s_1 is a constant shear magnitude below height h. At and above h, the profile becomes

$$\begin{aligned} u(z) &= u_b + s_2(z - h), \\ v(z) &= v_b + s_1 h, \end{aligned} \tag{2}$$

where s_2 is a constant shear magnitude above height h. The wind velocity is then held constant above 6 km AGL. The shape of this wind profile closely resembles observed wind profiles from supercell environments (Markowski et al. 2003; Parker 2014), which often feature an abrupt nearly 90° "kink" at low levels and approximately unidirectional shear above this "kink." We set u_b and v_b in all profiles to the approximate average values of -1.5 and 3.5 m s^{-1}, respectively, from the tornado report proximity sounding database of Smith et al. (2012), Thompson et al. (2012), and Coffer et al. (2019), and set h to 1000 m. Variations in the ground-relative wind may influence mesocyclones and tornadogenesis via the relationship between ground-relative winds and the frictional generation of low-level horizontal vorticity (Flournoy and Rasmussen 2021; Fischer and Dahl 2022). We have neglected such variations in the ground-relative wind to limit the scope of our study.

To provide a contrast with the L-shaped wind profile which did not have curvature above 1 km AGL, the second hodograph shape featured curvature everywhere below 6 km AGL. This wind profile was prescribed by the following formulas:

$$\begin{aligned} u(z) &= u_b - a_1 \cos\left(\pi \frac{z}{a_2}\right), \\ v(z) &= v_b + a_1 \sin\left(\pi \frac{z}{a_2}\right), \end{aligned} \tag{3}$$

below height h, and

$$\begin{aligned} u(z) &= u_b - a_1 \cos\left[\pi\left(\frac{h}{a_2} + \frac{z-h}{z_t-h}\frac{a_2-h}{a_2}\right)\right], \\ v(z) &= v_b + a_1 \sin\left[\pi\left(\frac{h}{a_2} + \frac{z-h}{z_t-h}\frac{a_2-h}{a_2}\right)\right], \end{aligned} \tag{4}$$

above h, where $z_t = 6000$ m. These equations produce a half-circle-shaped hodograph (denoted in the simulation name with a "C," Fig. 3) with different shear magnitudes below and above h, much like in the case of the L-shaped wind profile. This profile also has two free parameters: a speed a_1 that controls the "radius" of the hodograph, and a height a_2 that controls the dividing point on the hodograph circle between the shear layers below and above h.

To provide context for how we will vary our wind profiles to set up our experiment, we revisit the definition of SRH (assessed over depth h), which is

$$\mathrm{SRH} \equiv \int_{z=0}^{z=h} \omega_s |\mathbf{V}_{\mathrm{SR}}| dz = h\overline{\omega_s}\,\overline{|\mathbf{V}_{\mathrm{SR}}|} + h\overline{\omega_s' |\mathbf{V}_{\mathrm{SR}}'|} \approx h\overline{\omega_s}\,\overline{|\mathbf{V}_{\mathrm{SR}}|}, \tag{5}$$

where $\omega_s \equiv (\mathbf{V}_{\mathrm{SR}}/|\mathbf{V}_{\mathrm{SR}}|) \cdot \omega_H$ is the horizontal streamwise vorticity, $\mathbf{V}_{\mathrm{SR}}$ is the horizontal storm-relative wind vector, ω_H is the horizontal vorticity vector, overbars denote averages over depth h, and primes denote local departures from layer averages. All quantities in this equation represent the vertical wind

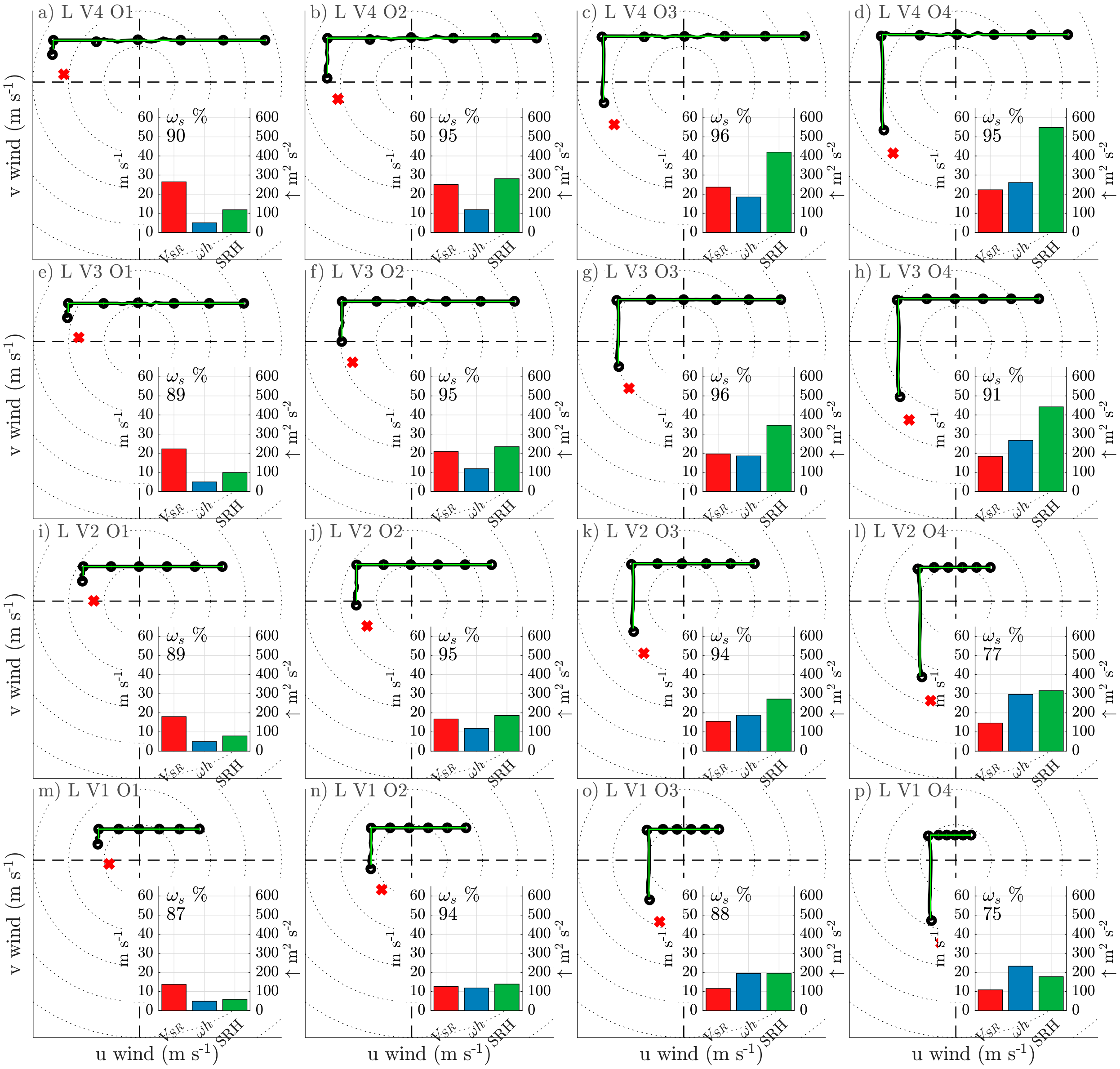

FIG. 2. Storm-relative hodographs for the 16 L simulations before (thin green lines) and after (thick black lines) the 15-h "spinup" period, with u and v wind on the x and y axes, respectively (m s^{-1}), and the origin representing the "Bunkers"-estimated right-mover storm motion. Dots are plotted on the hodograph curve from the surface to 6000 m AGL at intervals of 1000 m. Wind speed range rings are included every 10 m s^{-1}. ω_s increases from the leftmost column to the rightmost column, and V_{SR} increases from the bottom row to the top row. The red × denotes the location where the ground-relative wind is zero. Each panel contains a subpanel in the lower right showing V_{SR} (red; m s^{-1}), $\omega_s h$ (i.e., streamwise vorticity times h, blue, m s^{-1}), and SRH (green, m^2 s^{-2}). The quantities in the subpanel were computed using the adjusted profiles (i.e., after the 15-h spinup period). The horizontal streamwise vorticity percentage, defined as the layer average of the horizontal streamwise vorticity magnitude divided by the total horizontal vorticity magnitude, is listed in each subpanel.

profiles used to initialize simulations, and therefore represent a storm's "background environment." Hence, as was discussed in the introduction, SRH relates to the product of $\overline{\omega_s}$ and $\overline{|\mathbf{V}_{\mathrm{SR}}|}$, and the use of SRH in forecasting implicitly introduces $\overline{|\mathbf{V}_{\mathrm{SR}}|}$ as a predictor of tornadoes (which is why we are investigating this quantity here). We should note that the quantity $\overline{\omega_s'|\mathbf{V}_{\mathrm{SR}}'|}$, which represents the covariance of horizontal streamwise vorticity and horizontal storm-relative flow, also influences SRH. However, in situations when both ω_s and $|\mathbf{V}_{\mathrm{SR}}|$ are relatively uniform with height (such is the case in our model profiles), this covariance term is small and its influence on storm behavior can be neglected in our analysis.

In both the L and C wind profiles, the low-level $\overline{\omega_s}$ (hereafter simply ω_s) and $|\mathbf{V}_{\mathrm{SR}}|$ (hereafter V_{SR}) are determined independently of one another by varying s_1 and s_2 in the L profile, and a_1 and a_2 in the C profile. Each wind profile shape featured four

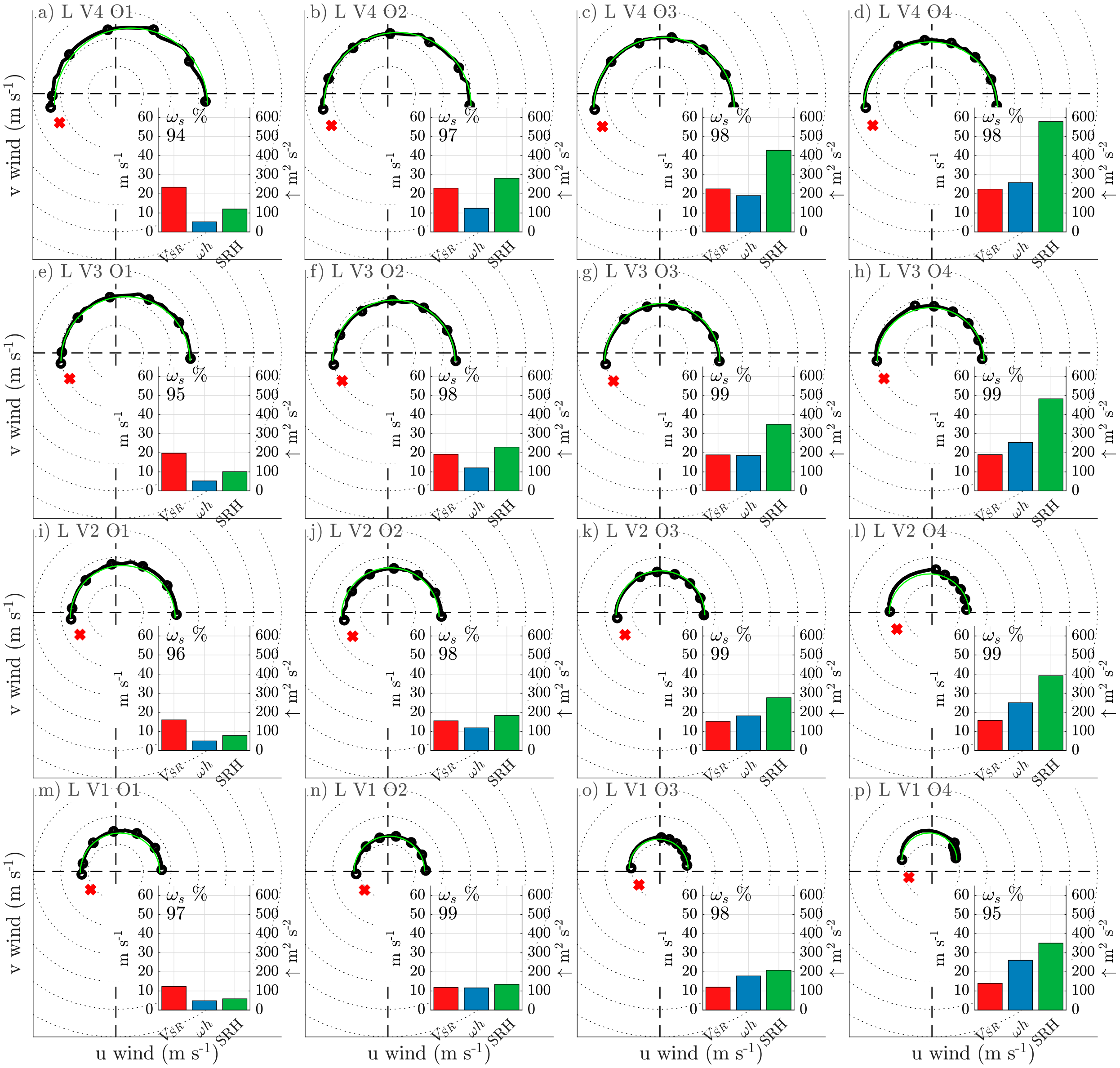

FIG. 3. As in Fig. 2, but for the C simulations.

different values of initial ω_s (denoted by an "O" in the simulation name), and four different values of initial V_{SR} (denoted by a "V" in the simulation name). Table 1 provides the precise initial values of both ω_s and V_{SR}. To obtain the s_1 and s_2 that corresponded to a given desired ω_s and V_{SR}, we simply searched for s_1 and s_2 (in the case of the L profile), and a_1 and a_2 values (in the case of the C profile) that minimized the difference between the ω_s and V_{SR} in our profiles and the desired values. This optimization procedure assumed that storm motion followed the Bunkers et al. (2000) "ID method" as a storm-motion estimate.

Values of ω_s and V_{SR}, computed using the actual storm motions in the simulations, differed somewhat from that of the Bunkers estimates used to set up the simulations. This is permissible in our experiment, given that the Spearman correlation coefficient between ω_s and V_{SR} among the simulations was 0.24 with a $p > 0.05$ determined from Student's t test, meaning that this correlation is not statistically different from zero and that we achieved our goal of varying ω_s and V_{SR} independently. Values of V_{SR} based on simulated storm motions ranged from 11.5 to 31.5 m s^{-1}, which is consistent with the range of typical supercell environments (i.e., >10 m s^{-1}; Droegemeier et al. 1993; Thompson 1998; Peters et al. 2020d). Bulk wind differences over the 0–1 km AGL layer ranged from 2.12 to 24.85 m s^{-1}, which is roughly consistent with the ranges in supercell environments shown in Fig. 9 of Thompson et al. (2003). Hence, the characteristics of our wind profiles generally reflect that of observed supercell environments.

TABLE 1. The range of 0–1 km AGL mean ω_s and 0–1 km AGL mean V_{SR} used to initialize simulations.

Wind attribute	Value
O1	$\omega_s = 0.25 \times 10^{-2}$ s^{-1}
O2	$\omega_s = 1.00 \times 10^{-2}$ s^{-1}
O3	$\omega_s = 1.75 \times 10^{-2}$ s^{-1}
O4	$\omega_s = 2.5 \times 10^{-2}$ s^{-1}
V1	$V_{SR} = 14$ m s^{-1}
V2	$V_{SR} = 18$ m s^{-1}
V3	$V_{SR} = 22$ m s^{-1}
V4	$V_{SR} = 26$ m s^{-1}

Because of the inclusion of parameterized surface drag and a fictitious wind balance in our simulations, there was inevitably some drift in the model vertical wind profile from the initial analytic profiles during the 15-h spinup period, and over the course of a 3-h simulation with active convection. The initial drift during the 15-h spinup period was very subtle (cf. the green to black lines in the hodographs in Figs. 2 and 3), and did not appreciably change the profile shapes or ω_s and V_{SR} magnitudes. We also acknowledge that the inclusion of a fictitious wind balance can lead to spurious vorticity generation. Once again, this subtle spurious effect is unlikely to affect our conclusions given our focus on low-level mesocyclones, rather than the early stages of tornado formation.

The naming convention uses the V and O values in Table 1. For instance, the simulation with the C wind profile, $V_{SR} = 22$ m s^{-1}, and $\omega_s = 2.5 \times 10^{-2}$ s^{-1} is referred to as the C V3 O4 simulation. These various combinations resulted in 32 unique vertical wind profiles, and consequently 32 simulations. Hodographs for the L and C wind profiles are shown in Figs. 2 and 3, respectively, with various vertical wind profile diagnostics (e.g., SRH) for each wind profile listed in the subpanels.

c. *Quantifying storm attributes*

Analyses that are presented later required that we track the primary right-moving supercell updraft within the domain, which we accomplished with the following algorithm. First, we computed the 1–3 km AGL average w, which we call w_{mean}. Second, grid points within w_{mean} were zeroed out if their 1–3 km AGL average vertical vorticity ζ_{mean} was negative. Third, we identified continuous regions of $w_{\text{mean}} > 3$ m s^{-1}. Fourth, we applied a Gaussian smoother with a radius of influence of 7.5 km to w_{mean}, to create w_s, where the subscript s denotes "smoothed." Finally, the "updraft of interest" was assigned to the continuous region of $w_{\text{mean}} > 3$ m s^{-1} that contained the maximum value of w_s. The updraft centroid at each time was defined as the average x and y location of all grid points contained within the updraft area. Finally, a Gaussian filter was applied to the position time series with a temporal radius of influence of 10 min to smooth the position time series. This method reliably tracked what we subjectively determined to be the most intense right-moving storm within each simulation. Time series of storm motion were computed using a centered-in-time finite difference that used filtered storm positions in 1 min model output.

Within the tracked updrafts, we quantify the following mesocyclone attributes (each with relevance to past research and forecasting):

- *Mesocyclone radius* R_m (i.e., the radius of rotating updraft), defined using the area A_m of the contiguous horizontal extent of ζ and w concurrently exceeding 1×10^{-2} s^{-1} and 3 m s^{-1}, respectively, such that $R_m \equiv \sqrt{A_m/\pi}$. This definition of mesocyclone extent is similar to that used in Trapp et al. (2017).
- *Net updraft circulation* c, defined as

$$c \equiv \iint \zeta dA, \tag{6}$$

where $\iint dA$ is the area integral within the continuous updraft area A at a given height. Circulation is often used in theory and numerical analyses of tornadoes.

- *Equivalent updraft rotational velocity* $\mathbf{v}$, defined as

$$\mathbf{v} \equiv \frac{c}{2\pi^{1/2}A^{1/2}}. \tag{7}$$

This quantity represents the rotation velocity that the updraft would have along its periphery if it were circular. This quantity is relatable to forecasting and "nowcasting," given that rotational speed can be derived from Doppler radial velocity data.

- *Average updraft vertical vorticity* $\overline{\zeta}$, defined as

$$\overline{\zeta} \equiv \frac{c}{A}. \tag{8}$$

Vertical vorticity is commonly used in defining mesocyclone boundaries and assessing mesocyclone intensity.

- *Average updraft helicity density* UH, defined as

$$\text{UH} \equiv \frac{1}{A}\iint w\zeta dA. \tag{9}$$

UH is a popular metric for mesocyclone intensity in forecasting and past theoretical analyses.

We experimented with a reasonable range of alternative w thresholds (i.e., 1, 5, 10 m s^{-1}) used to define updrafts, ζ thresholds (i.e., 0.25×10^{-2}, 0.5×10^{-2}, 2.0×10^{-2} s^{-1}) used to define the mesocyclone, and heights (i.e., 500, 1500, 2000 m) at which to assess quantities. All of these parameters gave similar results (not shown) to those described in the next section. Finally, to draw a physical connection between mesocyclone attributes and tornadoes, we analyze the horizontal maximum in w at 1 km AGL as a proxy for the potential for vertical stretching of vertical vorticity by the updraft.

The variables ω_s and V_{SR}, which depend on storm motion, were computed at each output time using the tracked storm motion at that time and the initial model wind profile (which represents the far-field environment). These quantities were vertically averaged over the lowest 1 km AGL of the atmosphere, and then temporally averaged from 45 min until either the end of the simulation or the last tracked updraft point.

d. *Identifying tornadoes*

The primary underlying motivation for studying mesocyclones is their connection to tornadoes. Hence, we also quantify tornado behavior in our simulations. Tornadoes were objectively defined as continuous regions of Okubo–Weiss (OW) parameter at the lowest model level (12.5 m AGL) exceeding 5×10^{-3} s^{-2} that contained ground-relative wind speeds exceeding the EF-0 threshold of 29 m s^{-1}. Tornado radius was defined from the tornado area $A_{\rm tor}$ as $\sqrt{A_{\rm tor}/\pi}$. In these calculations, $\mathrm{OW} \equiv -(\partial u/\partial y + \partial v/\partial x)^2 - (\partial u/\partial x - \partial v/\partial y)^2 + \zeta^2$ is positive in regions where the ζ magnitude exceeds the normal and shear strain magnitudes, which is characteristic of rotating fluids with closed circuit streamlines. We also evaluated OW thresholds ranging from 2.5×10^{-3} to 1×10^{-2} s^{-2} (not shown), and found our results to be relatively insensitive to the particular threshold used.

3. Results

a. *General attributes of the simulations*

There were two general outcomes for deep convection among the simulations. In the most common outcome, quasi-steady supercells with persistent rotating updrafts developed from the initial updraft nudging region, and persisted until the end of the simulation at 3 h. This was generally true for the V2–4, the L V1 O1, and L V1 O2 simulations, evidenced by relatively steady values of maximum domain w from 30 min onward through the end of the aforementioned simulations (Fig. 4). In contrast, supercell-like storms did develop in the V1, the L V2 O4, C V2 O1, and C V2 O4 simulations, but these storms were undercut by their outflow and eventually decayed by the end of the simulations, as evidenced by a peak and then a decline in maximum domain w (Fig. 4). Hence, like in the case of past modeling studies (Droegemeier et al. 1993; Peters et al. 2020d), a critical lower threshold of storm-relative flow appears necessary for sustained supercells to develop. We devote the remainder of quantitative analysis to understanding the influences of storm-relative flow on *sustained supercells*, and accordingly only include simulations whose updrafts were captured by our tracking method for up to 80 min after the initial forcing period ceased. This excludes the following simulations: L V1 O3, L V1 O4, L V2 O4, and the C V1 O1–4.

Roughly a third of the simulations produced tornadoes, which are evident as abrupt and sometimes persistent jumps in the magnitude of maximum surface ζ in Fig. 4, and are marked by green lines on the x axis. We ignore these tornadic periods when they occur within 20 min of the end of the forcing time period, due to spurious influences of the convection initiation method on tornadogenesis (Davies-Jones 2021). Tornadic simulations were generally grouped toward larger ω_s (i.e., the right-hand side of Fig. 4) and with less apparent sensitivity to $V_{\rm SR}$ (i.e., the rows in Fig. 4).

Composite radar and cold-pool characteristics show common characteristics of supercells in all simulations, including a general offset of precipitation toward the northwest, north, and northeast of the updraft, and hook echoes with accompanying rear-flank cold pools (Fig. 5). Consistent with the results of Peters et al. (2020d), updraft area appears to depend strongly on storm-relative flow, while showing comparatively little dependence on horizontal streamwise vorticity. Interestingly, there is a complex relationship between composite mesocyclone characteristics, horizontal streamwise vorticity, and storm-relative flow (Fig. 6). For instance, the most locally intense 1 km AGL ζ generally occurs with largest horizontal streamwise vorticity. Among the simulations with intermediary and small magnitudes of horizontal streamwise vorticity (i.e., O1–3), there is a subtle trend for *decreasing* ζ with increasing storm-relative flow (particularly in the L simulations), implying little connection or even an inverse relationship between maximum mesocyclone ζ magnitude and $V_{\rm SR}$. The patterns evident in this subjective analysis foreshadow quantitative trends in the simulations that will become apparent in the next subsection.

b. *Mesocyclone characteristics as a function of the storm environment*

We quantitatively evaluate our hypotheses via an exploration of correlations between updraft, mesocyclone, and environmental attributes. All reported correlation coefficients (CC) are Spearman rank correlations. Replicating our analysis with Pearson CC (not shown) yielded similar results to those shown below. We acknowledge that correlations themselves do not strictly signify a causal relationship between variables. Hence, we devote section 4 to exploring the physical connections responsible for the correlations identified in this section. We require that $p < 0.05$ from a Student's t test to consider a correlation to be statistically different from zero.

Consistent with our subjective analysis of Fig. 5, updraft radius and storm-relative flow were strongly correlated with a CC of 0.76 (Fig. 7a), whereas updraft radius and horizontal streamwise vorticity were poorly correlated (CC of 0.14, Fig. 7b). This result supports the part of H1 postulating that storm-relative flow should regulate updraft radius. The other part of H1 hinges on the connection between updraft radius and mesocyclone attributes hypothesized by Trapp et al. (2017). Consistent with our subjective analysis of Fig. 6, simulated mesocyclone radius was uncorrelated with simulated updraft radius and storm-relative flow (Figs. 7c,d), whereas mesocyclone radius displays a significant CC of 0.77 with horizontal streamwise vorticity (Fig. 7e). These statistics demonstrate that mesocyclone area in our simulations is strongly tied to horizontal streamwise vorticity and comparatively insensitive to storm-relative flow or updraft radius.

An analysis of net updraft circulation reveals similar patterns of correlations. Both updraft radius and storm-relative flow were weakly positively correlated with updraft circulation (Figs. 7f,g). In contrast, the CC of horizontal streamwise vorticity with updraft circulation was 0.87 (Fig. 7h), suggesting a strong physical connection between these two variables. This pattern of correlations continues with rotational velocity, with statistically insignificant correlations present between updraft radius, storm-relative flow, and rotational velocity (Figs. 7i,j), and a strong statistically significant CC of 0.86 present between horizontal streamwise vorticity and rotational

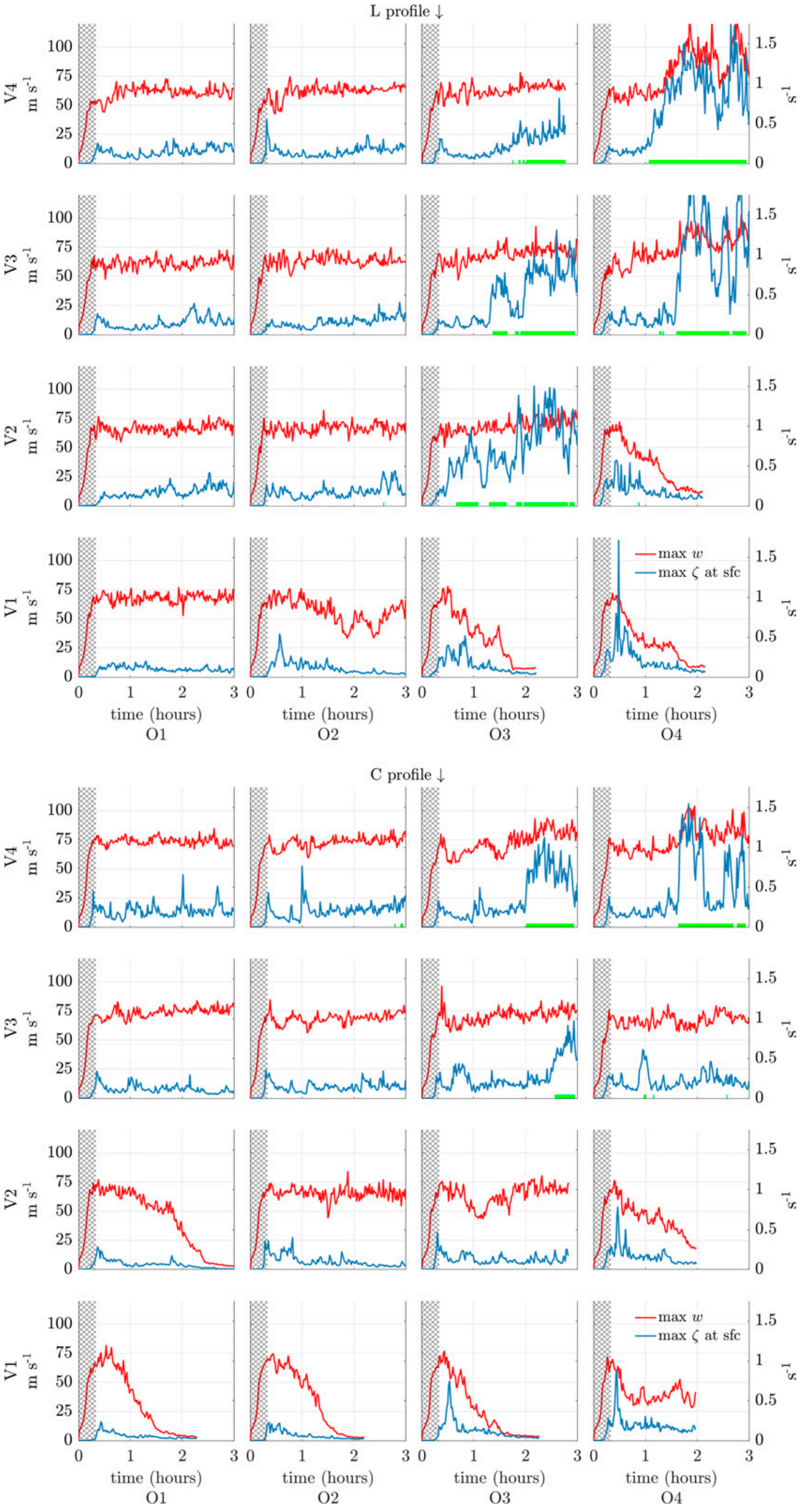

FIG. 4. Time series of maximum domain w (red, m s^{-1}, left y axis) and maximum surface ζ (blue, s^{-1}, right y axis), with the initial forcing period hatched. Each panel represents a separate simulation with columns and rows corresponding to initial ω_s and V_{SR}, respectively. The L wind profile simulations are shown in the top group, and the C wind profile simulations are shown in the bottom group. Green lines along the x axes mark tornadic periods.

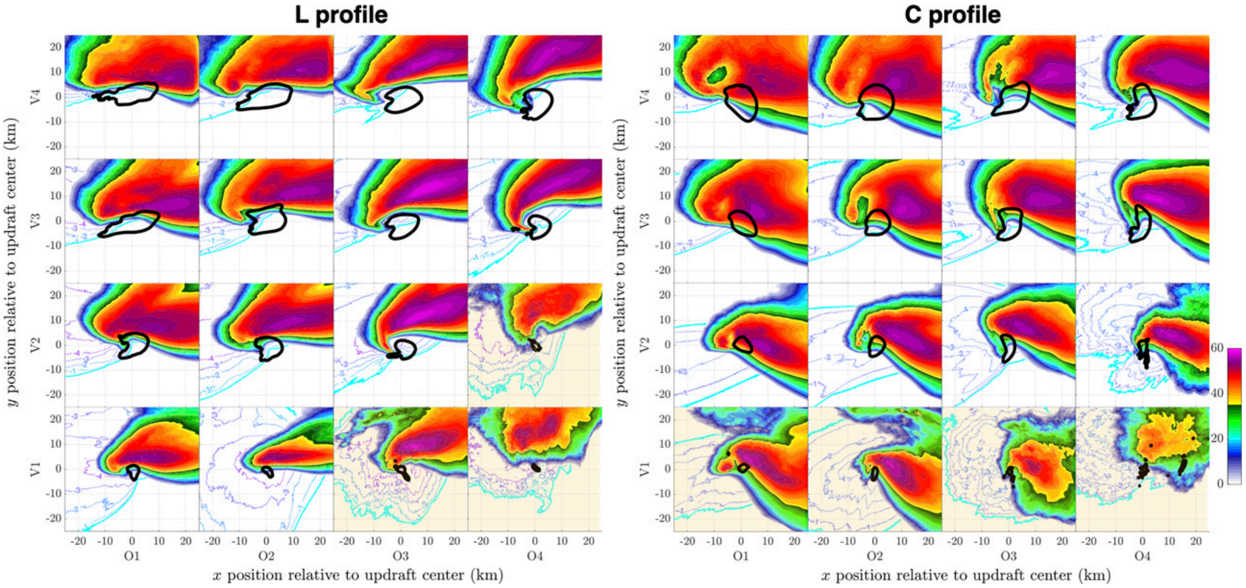

FIG. 5. Composites centered on the 1 km AGL updraft centroid of 1 km AGL simulated logarithmic radar reflectivity factor (shading, dB*Z*), surface potential temperature θ perturbation (blue contours, K), and the 1 km AGL 3 m s^{-1} *w* contour (thick black line). Composites were computed from 45 min through 3 h, with *data* output every 1 min. In the case of simulations that did not produce sustained supercells, composites were temporally averaged from 45 min until the last instance that our tracking algorithm identified an updraft. *x* and *y* axes ticks are the *x* and *y* distances from the updraft center (in km), respectively. Each panel represents a separate simulation with columns and rows corresponding to initial ω_s and V_{SR}, respectively. (left) The L wind profile simulations; (right) the C wind profile simulations. Panels faded yellow correspond to simulations that were excluded from correlation analyses because their storms did not survive for longer than 80 min.

velocity (Fig. 7k). Correlations of updraft radius and storm-relative flow with average updraft vertical vorticity (Figs. 7l,m) were statistically significantly negative in a similar manner to our subjective assessment of Fig. 6. In contrast, the relationship between horizontal streamwise vorticity and average updraft vertical vorticity is large and positive, with a CC of 0.70 (Fig. 7n). The story is the same for UH, which was strongly correlated with horizontal streamwise vorticity (Fig. 7q, CC = 0.89), and

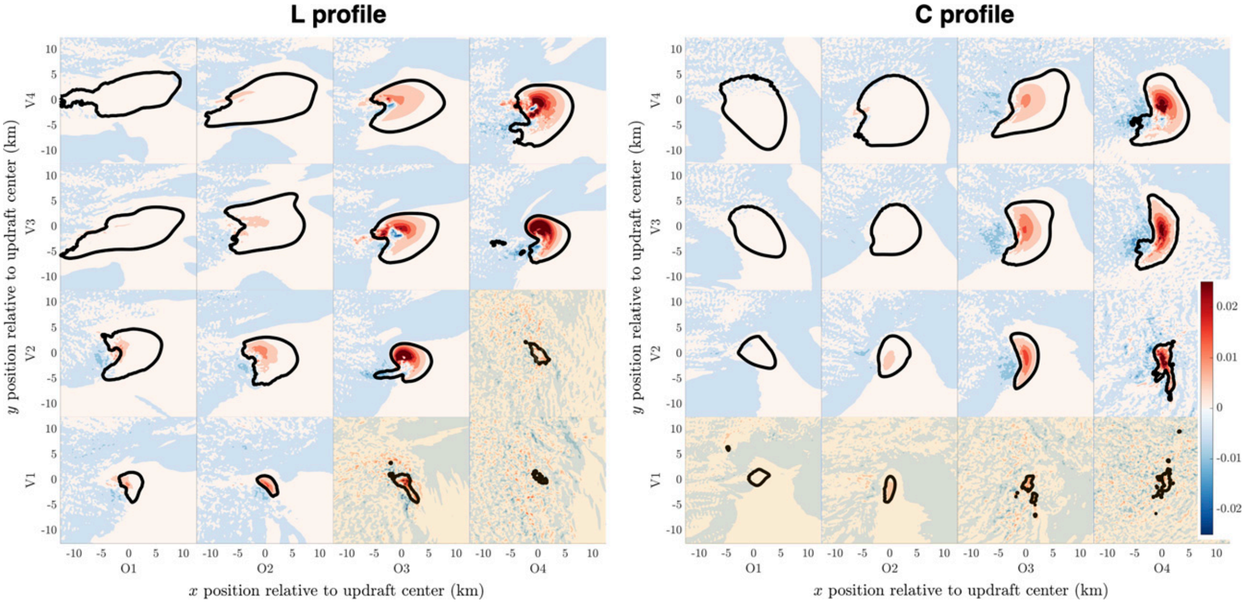

FIG. 6. As in Fig. 5, but showing 1 km AGL ζ (shading, s^{-1}) and the 1 km AGL 3 m s^{-1} *w* contour (thick black line). Panels are zoomed in on the updraft relative to Fig. 5.

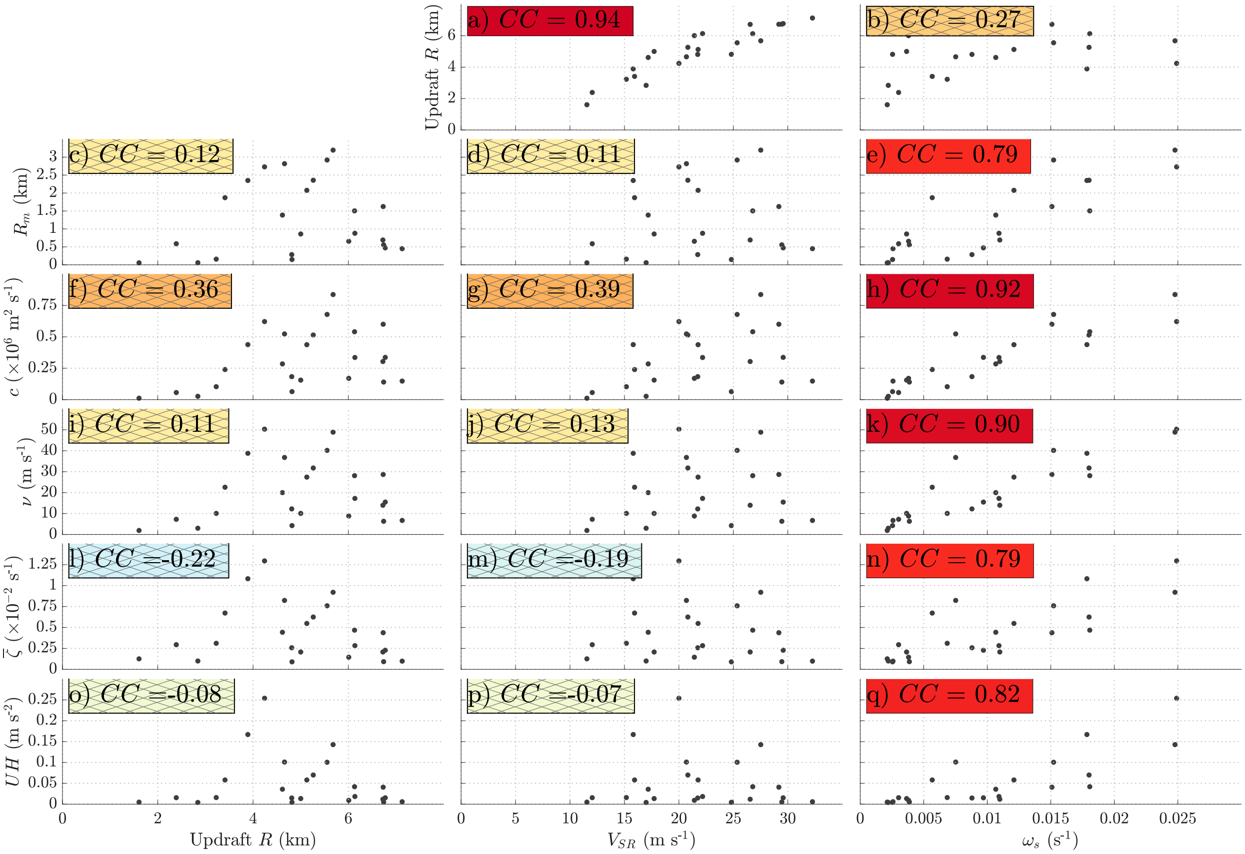

FIG. 7. Scatterplots of predictors (columns) for updraft and mesocyclone attributes (rows). Each dot represents a temporal average from a given simulation from 45 min through 3 h. Spearman correlation coefficients CC are shown in panel labels, with the panel label color reflecting the relative magnitude of CC (reds are positive, blues are negative). Hatched CC were not statistically significantly different from zero.

uncorrelated with updraft radius (Fig. 7o) and storm-relative flow (Fig. 7p).

The statistically insignificant correlations of mesocyclone characteristics with storm-relative flow potentially hide weak physical relationships whose signal is swamped by the strong relationship between variables and horizontal streamwise vorticity. To better understand the nature of storm-relative flow influences on updrafts, we further isolated the influence of storm-relative flow from that of horizontal streamwise vorticity by computing a linear trend line (not shown) between horizontal streamwise vorticity and each variable, and then removed this trend line from the data (referred to as "detrending"). We then recomputed correlations of the resulting detrended variables with updraft radius and storm-relative flow. The resulting relationship of updraft radius and storm-relative flow with detrended mesocyclone radius (Figs. 8a,b) and detrended rotational velocity (Figs. 8e,f) remained statistically insignificant. In contrast, the relationship of updraft radius and storm-relative flow with detrended circulation was more positive than in the case of the nondetrended circulation (Figs. 8c,d). This indicates that for a given horizontal streamwise vorticity magnitude, stronger storm-relative flow (wider updrafts) generally results in greater circulation than weaker storm-relative flow (narrower updrafts). An even stronger statistically significant negative relationship was present between updraft radius and storm-relative flow with detrended average vertical vorticity (Figs. 8g,h) and UH (Figs. 8i,j). This indicates that for a given horizontal streamwise vorticity, stronger storm-relative flow (wider updrafts) generally results in weaker overall vertical vorticity magnitudes than weaker storm-relative flow (narrower updrafts).

c. *Tornado characteristics as a function of mesocyclone characteristics and the storm environment*

Since the underlying motivation for studying mesocyclone intensity relates to tornado prediction, we explore how the trends in mesocyclone behavior from the previous subsection correspond to trends in tornado behavior. First, we establish a dynamical link between mesocyclone attributes and tornadoes by examining correlations between mesocyclone attributes and temporal averages of 1 km AGL maximum vertical velocity $w_{\max}$ (Figs. 9a–f; with tornadic time periods excluded). Updraft radius showed no statistically significant connection to $w_{\max}$ (Fig. 9a), whereas all mesocyclone attributes were strongly correlated with $w_{\max}$ (Figs. 9b–f). This suggests that storms with faster rotating mesocyclones (whichever way rotation

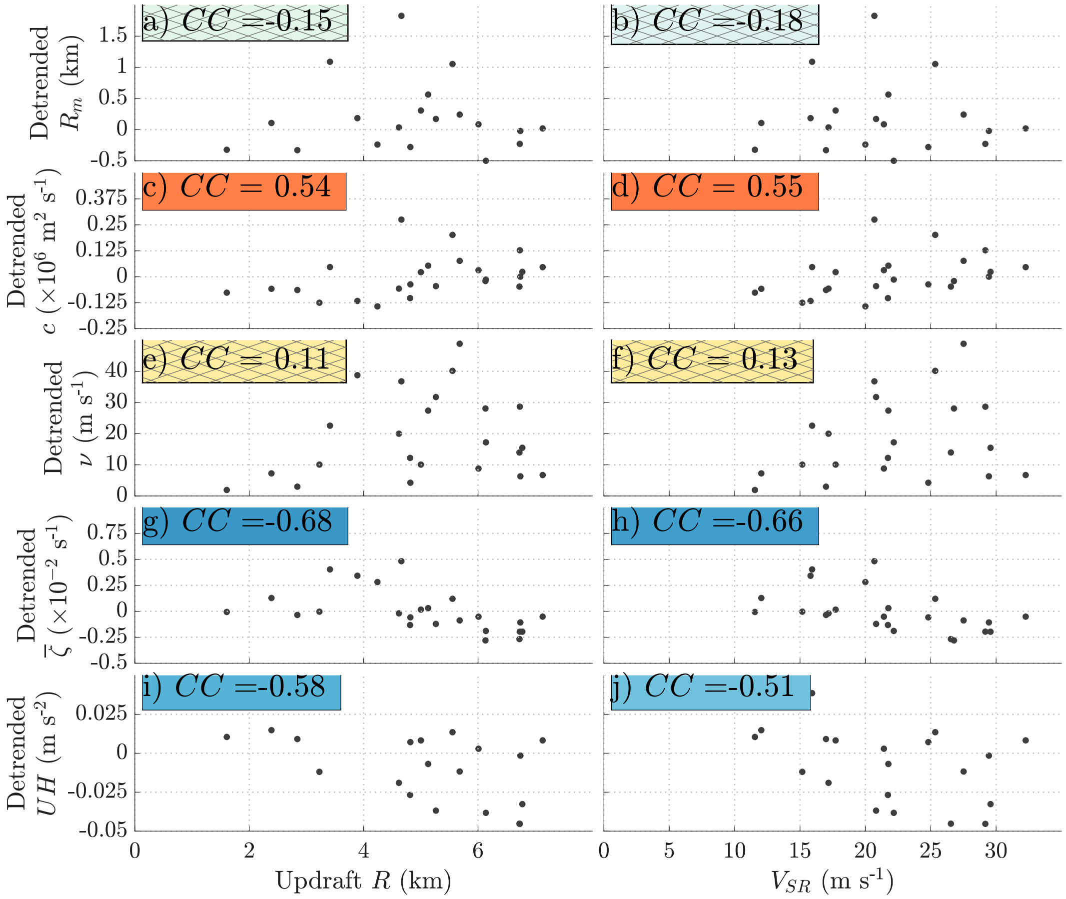

FIG. 8. Analogous layout to Fig. 7, but for mesocyclone attributes that are detrended with respect to horizontal streamwise vorticity.

was measured) featured larger near-ground vertical accelerations than in storms with slower rotating mesocyclones, and accordingly a greater potential for stretching of near-surface vertical vorticity. A similar trend is evident in Peters et al. (2020d) (Fig. 10 in that study). Interestingly, while the results of Peters et al. (2020d) agree with ours in that horizontal streamwise vorticity had a larger influence on low-level vertical velocity than storm-relative flow, these trends in Peters et al. (2020d) reversed in the upper troposphere with storm-relative flow largely determining overall updraft maximum vertical velocity. Hence the controls on low-level and overall updraft maximum vertical velocity differ from one another.

Next, we consider four tornado attributes: the length of time during which a tornado was present in a simulation (referred to as "tornado hours"), maximum ground-relative wind speed ("max V_{sfc}") within the tornado, the maximum tornado radius, and the 90th percentile of tornado radius. Tornado hours are set to zero for nontornadic storms. All other tornado-related quantities are omitted for nontornadic storms.

None of the tornado attributes were statistically significantly correlated with updraft radius (Figs. 9g,m,s,y). This includes tornado width (Figs. 9s,y), which casts doubt on the connection between updraft and tornado width hypothesized by Trapp et al. (2017), among our simulations at least. The length of time a storm was tornadic showed the strongest correlation with circulation and rotational velocity (Figs. 9i,j), with slightly lesser, albeit comparable, correlations with mesocyclone radius, average vertical vorticity, and UH (Figs. 9h,k,l). Maximum surface wind speeds showed the strongest correlation with circulation (Fig. 9o) and rotational velocity (Fig. 9p), and slightly lesser, albeit statistically significant, correlations with mesocyclone radius (Fig. 9n), average vertical vorticity (Fig. 9q), and UH (Fig. 9r). In contrast with the aforementioned tornado characteristics, the only mesocyclone attribute that was statistically significantly correlated with tornado radius was circulation, at a modest CC = 0.57 (Fig. 9u). All other correlations between mesocyclone attributes and tornado width were small and statistically insignificant (Figs. 9t,v–x,z–dd). In general, circulation and rotational velocity are the mesocyclone attributes most closely tied to the amount of time a storm was tornadic, and the intensity of the tornadoes that did form, whereas tornado radius seems to have little connection with the attributes of the mesocyclone that we have studied.

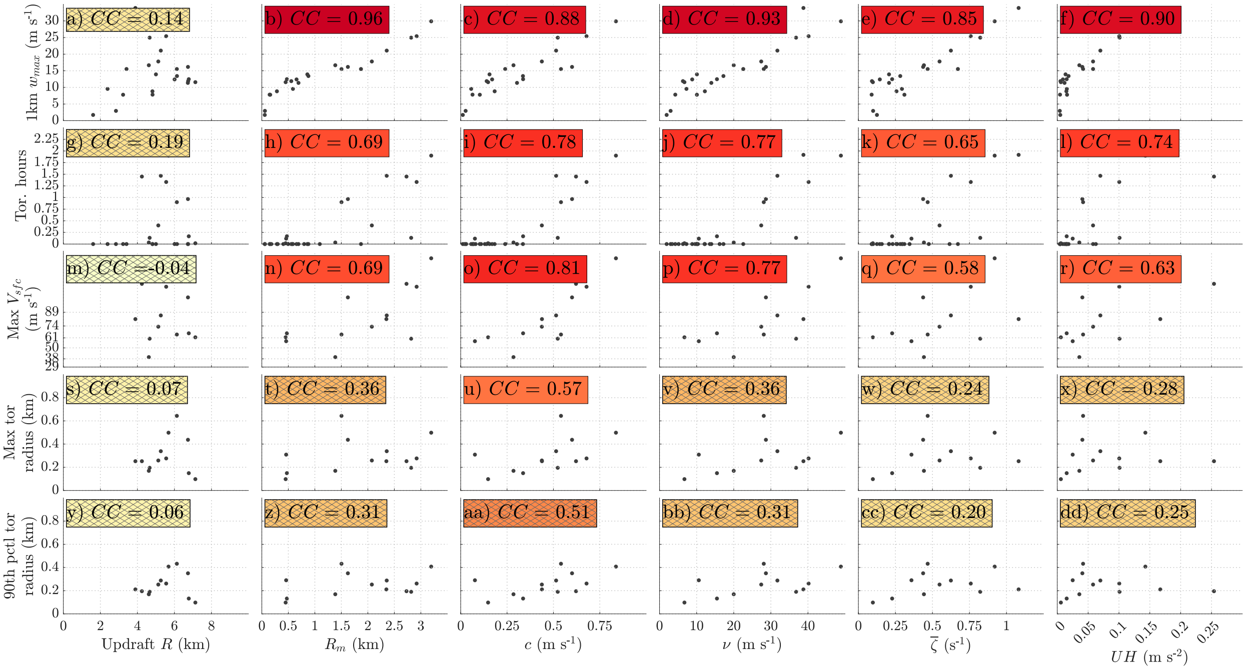

FIG. 9. Analogous layout to Fig. 7, but for mesocyclone attributes (columns) as predictors for tornado attributes (rows).

4. Theoretical interpretation of the results from simulations

The physical explanation for an absent or weak inverse relationship of mesocyclone properties with storm-relative flow and updraft width relates to the slant angle $\phi = \tan^{-1}(w/v_{\mathrm{SR}})$ of parcels relative to the horizontal as they enter the mesocyclone. We demonstrate this using a steady-state Boussinesq Beltrami flow model (e.g., Davies-Jones 2008) to represent the behavior of the air entering below the 1 km AGL updraft. In Beltrami flow, vorticity is purely streamwise such that

$$\mathbf{V}_{\mathrm{SR}} = \lambda \mathbf{\Omega}, \tag{10}$$

where $\mathbf{V}_{\mathrm{SR}}$ is the three-dimensional storm-relative flow vector, $\mathbf{\Omega}$ is the three-dimensional vorticity vector, and λ is a constant that is referred to as the "abnormality." The Beltrami flow assumption is a reasonable approximation in our simulations, given that the horizontal vorticity below 1 km AGL in the initial model vertical wind profiles of the simulations that produced sustained supercells was nearly purely streamwise (e.g., Figs. 2 and 3). For air that begins in the cloud's far-field environment with no vertical velocity, a storm-relative wind speed of V_{SR}, and a horizontal streamwise vorticity of ω_s, we may use Eq. (10) to write

$$V_{\mathrm{SR}} = \lambda \omega_s. \tag{11}$$

In the updraft core (denoted by subscript c), we may use Eq. (10) to write

$$\zeta_c = \lambda w_c. \tag{12}$$

Combining Eqs. (11) and (12) to eliminate λ yields

$$\zeta_c = \omega_s \frac{w_c}{V_{\mathrm{SR}}}. \tag{13}$$

While the above equation explicitly contains storm-relative flow, it does not offer much definitive insight into its influence on the mesocyclone due to the coincident presence of w_c in the equation, which may vary independently of V_{SR}.

To eliminate w_c, we note that

$$\frac{w_c}{V_{\mathrm{SR}}} = \frac{|\mathbf{V}_{\mathrm{SR}}|}{V_{\mathrm{SR}}} \tan\phi_c \approx \tan\phi_c, \tag{14}$$

where we have linearized the equation by assuming that the three-dimensional storm-relative wind speed $|\mathbf{V}_{\mathrm{SR}}|$ remains equal to the initial storm-relative wind speed in the far-field environment V_{SR}, such that $|\mathbf{V}_{\mathrm{SR}}|/V_{\mathrm{SR}} = 1$. Combining Eq. (13) with Eq. (14) yields

$$\zeta_c = \omega_s \tan\phi_c. \tag{15}$$

A similar expression was obtained in Davies-Jones (2022), his Eq. (88). We may further simplify this expression using the Boussinesq continuity equation, which is written in its azimuthally averaged cylindrical form as

$$\frac{\partial r u_r}{\partial r} + \frac{\partial r w}{\partial z} = 0, \tag{16}$$

where u_r is the azimuthally averaged radial wind component. Radially integrating from the updraft center at $r = 0$ to the updraft edge at $r = R$ and vertically integrating from the ground to the height h of the mesocyclone we are examining yields

$$2h\widehat{u_r} + R\overline{w} = 0, \tag{17}$$

where $-\widehat{u_r}$ is the area average of inflowing air across the updraft edge (i.e., “inflow”), and $\overline{w}$ is the horizontal average of w at height h.

Past studies (e.g., Peters et al. 2019, 2020a) have shown that the low-level storm-relative wind V_{SR} scales proportionally to $\widehat{u_r}$. Hence, we assume that $\widehat{u_r} = -\sigma V_{\mathrm{SR}}$, where $0 < \sigma < 1$ is a constant. Furthermore, we assume that $\overline{w}$ scales with w_c such that $\overline{w} = \alpha w_c$ for $0 < \alpha < 1$ (this assumption is commonplace in the cumulus parameterization community; e.g., Morrison 2017; Morrison and Peters 2018). Applying these assumptions to Eq. (17) and rearranging yields

$$\frac{w_c}{V_{\mathrm{SR}}} \approx \tan\phi_c \approx \frac{2h\sigma}{R\alpha}. \tag{18}$$

Equation (18) tells us that, to first approximation, the ascent angle ϕ_c of the storm-relative airstream scales inversely with the updraft radius, irrespective of the strength of the low-level updraft and the speed of storm-relative flow at the updraft edge (i.e., inflow). This is because a strong low-level updraft must feature commensurately strong low-level horizontal inward accelerations, relative to a weak low-level updraft, to satisfy mass continuity. Because these horizontal and vertical accelerations scale with one another, their respective influences on ϕ approximately cancel one another in the ratio w_c/V_{SR}, and hence these terms vanish from the equation.

Combining Eqs. (18) and (15) yields

$$\zeta_c = \frac{2h\sigma}{\alpha}\frac{\omega_s}{R}. \tag{19}$$

This equation tells us that the vertical vorticity in the mesocyclone scales proportionally to the horizontal streamwise vorticity, and inversely with the updraft radius. The storm-relative flow has now dropped out of the equation, but implicitly remains present via its scaling with R (see our Fig. 7a). This scaling is supported by numerous previous studies (Warren et al. 2017; Peters et al. 2019, 2020c,a), along with in our simulations (Fig. 7a). Our interpretation of this equation will hinge on the assumptions that α, σ, and hence $2h\sigma/\alpha$ are constants. We will verify these assumptions shortly by assessing the right-hand side of Eq. (19) as a predictor of simulated mesocyclone characteristics.

An expression for R as a function of $\widehat{u_r}$ (again, the average radial flow across the updraft boundary) was derived in section 4 of Peters et al. (2019), Eq. (18) therein. In its full form, the expression from Peters et al. (2019) is quite complicated, but can be simplified to

$$R^2 = \frac{4\beta\widehat{u_r}H^2}{\alpha\mathrm{CAPE}_H}, \tag{20}$$

if we assume that the flow ascending through the core of our simulated supercell updrafts is approximately undiluted, which is a reasonable assumption in sustained supercells (e.g., Peters et al. 2019). Hence the entrainment-related Ω terms in Eq. (18) from Peters et al. (2019) vanish yielding Eq. (20). Here, H is the height that typically coincides with the height of maximum buoyancy [see Peters et al. (2019) for a specific definition], β is a constant, α holds the same definition in that study as it does here, $\mathrm{CAPE}_H \equiv \int_{z=\mathrm{LFC}}^{z=H} B_{\mathrm{AD}}\,dz = \widehat{B_{\mathrm{AD}}}H$, where B_{AD} is the buoyancy for an air parcel originating in the storm’s effective inflow layer (EIL; Thompson et al. 2007) that is lifted adiabatically, LFC is the level of free convection, and $\widehat{B_{\mathrm{AD}}}$ is B_{AD} averaged from the LFC to H. Using $\widehat{u_r} = -\sigma V_{\mathrm{SR}}$ [as we did to derive Eq. (18)] and simplifying, we may write Eq. (20) as

$$R = \tau V_{\mathrm{SR}}, \tag{21}$$

where $\tau \equiv \sigma\left(\sqrt{4\beta/\alpha}\right)\left(H/\sqrt{\mathrm{CAPE}_H}\right)$ relates to the time scale of ascent of an updraft parcel. Outside of tornadic periods, it is reasonable to assume that H and CAPE_H were invariant among the simulations that produced sustained supercells. Hence, τ is approximately constant and the scaling between R and V_{SR} is approximately linear (see Fig. 7a). Combining Eq. (20) with Eq. (19) yields

$$\zeta_c = \frac{2h\sigma}{\alpha\tau}\frac{\omega_s}{V_{\mathrm{SR}}}, \tag{22}$$

which affirms that ζ_c should scale inversely with V_{SR}, and is consistent with the negative relationship that we found in the simulations (e.g., Fig. 8h).

The schematic in Fig. 10 illustrates the physical reason for the relationships in Eqs. (19) and (22). In an environment with weak storm-relative flow below height h and a small updraft radius, the storm-relative airstream below height h must turn upward at a steep slant angle ϕ_1 to feed the low-level updraft (Fig. 10a). In contrast, when storm-relative flow is large, parcels travel a greater horizontal distance for a given vertical displacement, thereby achieving a smaller slant angle ϕ_2 (Fig. 10b). Because $\phi_1 > \phi_2$, the narrower updraft amid weaker storm-relative flow will project more initially horizontal streamwise vorticity into the vertical direction, and thereby achieve a larger ζ magnitude than the wider updraft amid stronger storm-relative flow.

To show evidence in support of our theoretical exercise, in each simulation we released a total of 50 000 trajectories inline with model integration using the built in CM1 software, which integrates forward in time with a third-order Runge–Kutta scheme. Initial y locations of trajectories ranged from −25 to 25 km at intervals of 100 m, z locations ranged from 40 to 4040 m at intervals of 40 m, and x locations were specified as $x(z) = 40\,000 \times u_0(z)/u_0(z_b)$, where u_0 is the initial model vertical u-wind profile and z_b is the height of the lowest scalar model level (12.5 m AGL). This range of initial trajectory locations was meant to optimize the number of trajectories entering storms’ 1 km AGL updrafts. We began trajectory integration at these locations 75 min into the simulations. To be considered a participant in the 1 km AGL updraft, we required that trajectories reach 1 km AGL with $w \geq 3\ \mathrm{m\ s^{-1}}$. Slant angle ϕ relative to the horizon (in degrees) was defined as $(180/\pi)\mathrm{a\,tan\,2}[w, V_{\mathrm{SR}}(t)]$, where $V_{\mathrm{SR}}(t)$ is the instantaneous

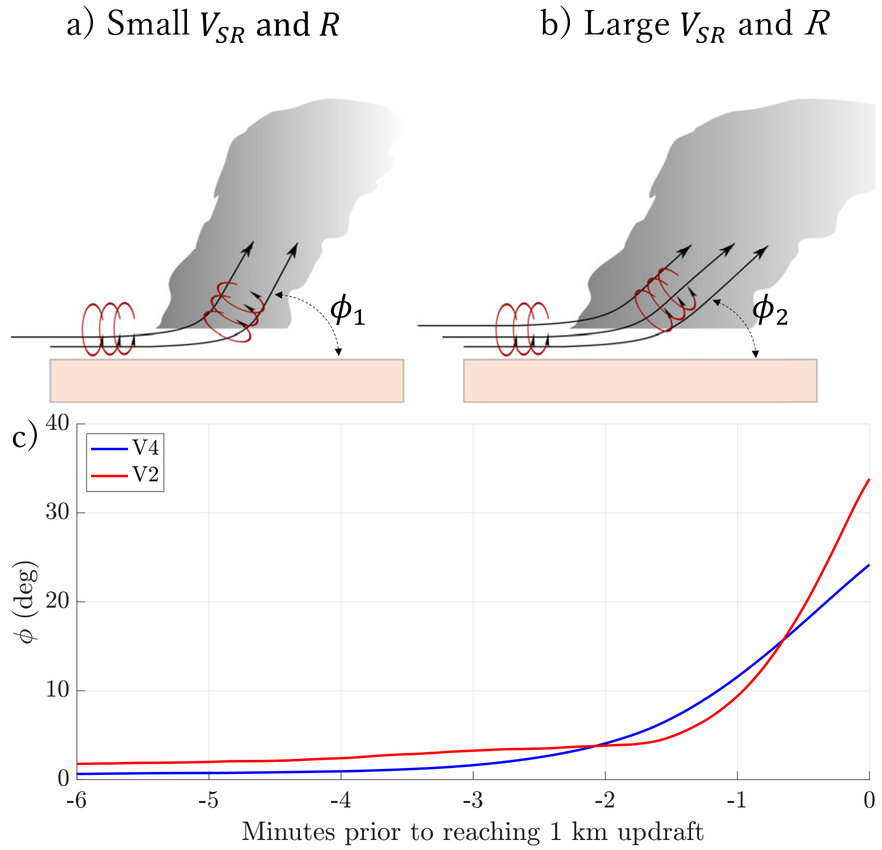

FIG. 10. (a),(b) Schematic illustrating the effect of V_{SR} on mesocyclogenesis. Black curved streamlines represent storm-relative flow, with the relative number of streamlines representing the storm-relative flow magnitude. Red circular arrows represent horizontal streamwise vorticity. Gray shaded regions denote the cloudy updraft region of a supercell. ϕ is the slant angle of parcels relative to the horizontal. The scenario in (a) leads to larger vertical vorticity than that in (b). (c) Averages of ϕ over all trajectories from a given simulation (y axis, degrees) as a function of time relative to 1 km AGL updraft entry (x axis, min) from the L O3 V4 simulation (blue line) and the L O3 V2 simulation (red line).

V_{SR} along a trajectory. Values of ϕ were then averaged over all updraft trajectories for each lag time prior to 1 km AGL updraft entry. The difference in slant angle as a function of storm-relative flow along these trajectories is demonstrated in Fig. 10c, wherein average slant angles of parcels entering the low-level updraft are less in the L 03 V4 simulation, which had strong storm-relative flow, than in the L 03 V2 simulation, which had weaker storm-relative flow.

Equation (19) indicates that vertical vorticity should scale with horizontal streamwise vorticity, which is indeed the case with a CC of 0.79 between these variables (Fig. 11a). Second, Eq. (18) suggests that ϕ should scale inversely with updraft radius, which is also true among simulated trajectories with a CC of −0.70 (Fig. 11b). Storm-relative flow follows a similar general trend to updraft radius, in terms of its negative relationship with ϕ (Fig. 11c). Indeed, a comparison of ϕ as a function of time prior to updraft entry in the L O3 V2 simulation, which featured weak storm-relative flow, to that of the L O3 V4 simulation, which featured comparatively strong storm-relative flow, shows patterns of slant angles that mimic that of the schematic (Figs. 10a–c). That is, steeper slant angles were present near the updraft edge in the V2 simulation than in the V4 simulation. Finally, our theoretical analysis hinges on the assumption that $\sigma/\alpha \approx$ constant in Eq. (19). If this assumption is valid, $h(\omega_s/R)$ (where h is our mesocyclone height of 1000 m AGL) and $\overline{\zeta}$ should have an approximately linear relationship with one another. Indeed, these two variables show a linear trend when plotted against each other with a Spearman CC of 0.87, and importantly a linear Pearson CC of 0.90 (Fig. 11d). This strongly supports our theoretical interpretation of mesocyclogenesis.

The expressions for ζ_c in Eqs. (19) and (22) can be used to corroborate the correlations of storm-relative flow with the other mesocyclone attributes in the simulations (i.e., Fig. 7). For instance, from the definition of circulation in Eqs. (6) and (21), we deduce that $c \sim \zeta_c R^2 \sim \zeta_c \tau^2 V_{\mathrm{SR}}^2$. This may lead one to incorrectly deduce that c should depend strongly (i.e., quadratically) on storm-relative flow. However, the inverse

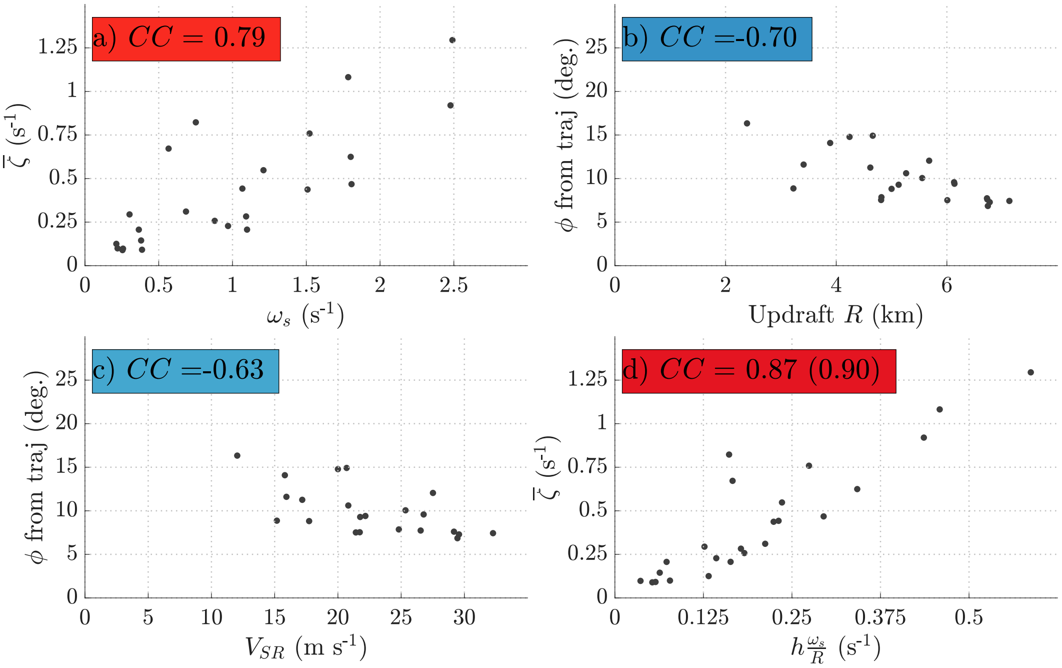

FIG. 11. (a) ω_s vs $\overline{\zeta}$ (as in Fig. 7n). (b) Updraft R vs ϕ along trajectories averaged between the first instance of $w = 1$ m s^{-1} and the 1 km AGL updraft. (c) As in (b), but with $V_{\rm SR}$ instead of R. (d) $h(\omega_s/R)$ vs $\overline{\zeta}$, with the linear Pearson CC shown in parentheses.

dependence of ζ_c on storm-relative flow is partially offsetting. This is demonstrated by combining Eqs. (6), (19), and assuming that $\overline{\zeta} = \alpha\zeta_c$ (i.e., average vertical vorticity scales with its value at the updraft center), to obtain

$$c = 2\pi h\sigma\omega_s\tau V_{\rm SR}. \tag{23}$$

Hence the dependence of c on $V_{\rm SR}$, while positive and linear, is relatively weak because of the aforementioned offsetting factors (e.g., Figs. 7g and 8d).

Similarly, from Eqs. (6), (7), and (21), we deduce that $\nu \sim \zeta\tau V_{\rm SR}$, which suggests that rotational velocity should scale linearly with storm-relative flow. However, this linear dependence is entirely offset by the inverse dependence of ζ_c on $V_{\rm SR}$. This is shown by combining Eq. (7) with Eq. (23) to obtain

$$\nu = h\sigma\omega_s. \tag{24}$$

Hence, there is no dependence of ν on $V_{\rm SR}$ in Eq. (24) or in the simulations (e.g., Figs. 7j and 8f).

Finally, solving Eq. (18) for w_c, and multiplying the resulting expression by Eq. (15) yields

$$\mathrm{UH}_c = w_c\zeta_c = (\tan^{-1}\phi_c)^2\omega_s V_{\rm SR}, \tag{25}$$

which is consistent with Eq. (90) in Davies-Jones (2022). This equation may lead us to deduce that UH scales positively with $V_{\rm SR}$. However, combining Eq. (25) with Eqs. (21) and (19) yields

$$\mathrm{UH}_c = \frac{4h^2\sigma^2}{\tau^2\alpha^2}\frac{\omega_s}{V_{\rm SR}}, \tag{26}$$

which affirms that UH_c, like ζ_c, should scale *inversely* with $V_{\rm SR}$, which is again supported by the negative relationship between detrended UH and R and $V_{\rm SR}$ in Figs. 8i and 8j.

5. Summary, conclusions, and closing discussion

In this article, we disentangle the influences of environmental horizontal streamwise vorticity and storm-relative flow—the primary constituents of storm-relative helicity—on low-level mesocyclone characteristics in simulated supercells. We consider the following hypotheses in our analysis:

- H1: Low-level layer-averaged storm-relative flow and environmental horizontal streamwise vorticity together (with comparable influence) regulate the mesocyclone size and intensity via their combined regulation of the mesocyclone width and the vertical vorticity magnitude.
- H2: Low-level layer-averaged storm-relative flow influences mesocyclones insofar as a critical lower threshold of this quantity is needed in a given environment for a sustained supercell. However, assuming there is sufficient low-level layer-averaged storm-relative flow for a sustained supercell to exist, mesocyclone size and rotation are primarily regulated by the environmental horizontal streamwise vorticity magnitude.

Our general conclusions are as follows:

- Consistent with prior studies, a lower threshold of storm-relative flow is necessary for simulations to produce a sustained supercell.
- When storm-relative flow is large and updrafts are wide, vertically tilted horizontal streamwise vorticity is projected over a wider area, but with a lesser average magnitude than when these parameters are small. These factors generally offset one another, resulting in weak correspondence of storm-relative flow with updraft circulation and rotational velocity (the updraft attributes most connected with tornado behavior) within the range of storm-relative flow magnitudes that typifies supercell environments.
- Rather, simulated mesocyclone characteristics, including those strongly related to tornadoes, were primarily determined by horizontal streamwise vorticity (supporting H2 over H1).

Overall, our results provide clarity on the role (or lack thereof) of storm-relative flow in dictating supercell low-level mesocyclone characteristics, which had previously been difficult to disentangle due to interdependent environmental attributes. We argue that the skill of SRH in predicting tornadoes primarily originates from the connection between SRH and horizontal streamwise vorticity. This idea is supported by past proximity sounding analyses of tornado environments. For instance, McCaul (1991) found that both horizontal streamwise vorticity and SRH had similar correlations with tropical cyclone tornado characteristics. Markowski et al. (2003) showed that low-level vertical profiles of horizontal streamwise vorticity discriminated between significantly tornadic supercell environments and weakly tornadic or nontornadic supercell environments similarly to low-level SRH density. Nowotarski and Jensen (2013) showed that self-organizing maps of vertical profiles of horizontal streamwise vorticity were among the best predictors of significantly tornadic supercells, while those of SRH density were not. Further, predictive skill in distinguishing tornadic versus nontornadic supercells was nearly identical for 0–500 m average horizontal streamwise vorticity and 0–500 m SRH in Coffer et al. (2019) (included in their supplemental analysis). Future research efforts should investigate whether there are particular situations where horizontal streamwise vorticity offers an advantage over SRH, or vice versa.

a. *Relating our results to past observational studies of storm-relative flow and tornadoes*

The lack of influence of low-level storm-relative flow on mesocyclone and tornado attributes in our study is an apparent contradiction to the observational results of Coniglio and Parker (2020) and Coniglio and Jewell (2022), who showed larger storm-relative flow in tornadic versus nontornadic supercell environments. A possible reconciling explanation is that their results reflected local storm-generated enhancements to the storm-relative flow field. As a simple evaluation of this possibility in our simulations, we examined a point to the southeast of the updraft center in each simulation that experienced the largest instantaneous 0–2 km AGL mean vector bulk wind difference from the initial model wind profile (this point was typically 10–20 km from the updraft edge). The average magnitude of this difference was 29.4% as large as the initial wind speed in simulations that were tornadic for more than an hour, and 22.1% as large as the initial wind speed in simulations that were tornadic for less than an hour or nontornadic, and the difference in these percentages was statistically significant. This statistic hints that tornadic storms may accelerate their near-storm inflow to a greater degree than nontornadic storms.

However, Coniglio and Parker (2020) show that tornadic supercells have larger storm-relative flow as far as 80 km away from their updrafts than nontornadic supercells, which is beyond the typical range of local storm-induced accelerations from a single supercell updraft (e.g., Peters et al. 2022b). Potential alternative explanations are that environmental storm-relative winds above the height ranges considered here, or within differently shaped hodographs than those considered here, have important influences on tornadogenesis. While our results provide some important initial foundational understanding, the aforementioned discrepancy between our results and these observational studies suggest that future research efforts are needed to fully understand the influences of storm-relative flow on tornadogenesis.

b. *Relating our results to those of Trapp et al. (2017)*

Our results also apparently contradict those of Trapp et al. (2017, 2018), wherein those authors argued that updraft width, midlevel mesocyclone width, low-level mesocyclone width, and tornado width are all dynamically linked. We did find a strong statistically significant correlation between updraft width and mesocyclone width at 6 km AGL (not shown). However, our theoretical and modeling analysis shows no dynamical link between updraft width or mesocyclone width at 6 km AGL with mesocyclone width at 1 km AGL, which is a more relevant height to tornado formation than 6 km AGL. This lack of correlation between 1 and 6 km AGL mesocyclone radii in our simulations is likely a consequence of the prevalent participation of entrained midlevel air in midlevel mesocyclones (shown in Peters et al. 2020d), which had markedly different horizontal vorticity than the air below 1 km AGL in our simulations. We note that in the numerical modeling experiments of Trapp et al. (2017, 2018) that both the low-level shear, deep-layer shear, and consequently storm-relative flow, were varied together via their method of varying the low-level hodograph radius among their simulations to impart differences in shear magnitude. Thus, storm-relative flow and horizontal streamwise vorticity were correlated in their simulations, which regulated overall updraft width and low-level mesocyclone width, respectively, via separate mechanisms. This gave the false impression of a dynamical connection between updraft width and low-level mesocyclone width. We can replicate this spurious result by noting that the "hodograph radius" increases along the diagonal from the lower-left to upper-right simulations in our hodograph matrices (see Figs. 2 and 3) in a similar way to how hodograph radius was varied in the Trapp et al. (2017) simulations. Repeating our analysis with only these simulations on the diagonal yields a CC of 0.98 between updraft and 1 km AGL mesocyclone radius, giving the false impression that these features regulate one another.

Since mesocyclone radius showed strong connections to tornado wind speeds and longevity in our simulations, whereas updraft radius showed no connections to tornado characteristics, the dynamical connection between updraft width and tornado width proposed by Trapp et al. (2017) is also not supported by our simulations. In fact, tornado width in our simulations showed little connection to any mesocyclone or updraft attributes, which echoes the results of Coffer and Markowski (2018), Fischer and Dahl (2020), and Goldacker and Parker (2021). This apparent lack of connection between tornado radius and updraft attributes may be explainable if one considers the first-order dependence of tornado vortex radius on the swirl ratio $S \equiv \upsilon_r/w$ (e.g., Davies-Jones 1973), where υ_r is a rotational velocity. In principle, w and υ_r should relate to the flow from which the tornado emerges, which is typically thought to be air with downdraft origins near the updraft base. While w is directly controlled by the supercell's low-level updraft, υ_r likely relates to the ambient vertical vorticity within the outflow, which may be a difficult-to-predict parameter that depends on a multitude of kinematic and thermodynamic characteristics of a storm and its environment. This may render the prediction of tornado radius from updraft and environmental characteristics challenging. We should note that mesocyclone radius did show strong connections with *tornado wind speed*, supporting the observational connection between these two variables found in Sessa and Trapp (2020).

c. *Caveats to our experiment design*

A potential caveat raised by a reviewer of this paper is that because tornadoes undoubtedly contribute to the 1 km AGL vertical vorticity within the updraft, it is difficult to determine whether variations in mesocyclone attributes are the cause of, or are the result of, variations in tornado behavior. However, we believe that our theoretical analysis, which clearly corroborates the connections between a storm's environment and its mesocyclone, suggest that the storm's environment is the primary control on the trends in simulated mesocyclones evident in our simulations, rather than the presence or absence of a tornado.

We must also caution that the range of environments in our simulations was far smaller than the range of possible combined thermodynamic and wind environments experienced by real storms. While the theoretical analysis in section 4 allows us to tentatively generalize our conclusions beyond the limited scope of simulated environments, there are numerous possible extraneous complicating factors in real environments that were not considered in the theoretical framework. These extraneous factors include (but are not limited to) variations in cold-pool characteristics and intensity, baroclinic generation of horizontal streamwise vorticity, complex vertical variability in wind and shear, and storm mergers and environmental heterogeneity. For instance, Guarriello et al. (2018) showed that differences in outflow positioning can have noticeable influences on near-ground rotation, which they attributed to the positioning of near-ground circulation with favorable dynamic pressure accelerations from the low-level mesocyclone. Moreover, the influence of the wind profile on outflow positioning is also likely to be strongly influenced by thermodynamic environmental factors affecting cold-pool intensity (Brown and Nowotarski 2019), which were not explored here. An additional mechanistic explanation of their findings may relate to how cold pools affected the tilting of parcels as they entered the updraft.

The contributions of baroclinic horizontal streamwise vorticity (Rotunno and Klemp 1985) and streamwise vorticity currents (Orf et al. 2017; Schueth et al. 2021) to vertical vorticity within the low-level mesocyclone were not considered. Despite the well-known contribution to low-level mesocyclones by baroclinically generated vorticity, environmental horizontal streamwise vorticity and SRH have substantial skill at forecasting low-level mesocyclone characteristics and thus tornadoes (and is known to forecasters a priori), further evidenced by the correlations presented in this work. The degree to which the storm-generated component of horizontal streamwise vorticity contributes to low-level mesocyclone attributes will be explored in a future study. Regardless of these caveats, the results of this study have important implications for understanding the environmental attributes that predominately control low-level mesocyclones in supercells.

Acknowledgments. We thank Matthew Flournoy and two anonymous peer reviewers for their helpful feedback on an earlier version of this manuscript. J. Peters's and J. Mulholland's efforts were supported by National Science Foundation (NSF) Grants AGS-1928666, AGS-1841674, and the Department of Energy Atmospheric System Research (DOE ASR) Grant DE-SC0000246356. B. Coffer's and M. Parker's efforts were supported by the National Oceanic and Atmospheric Administration (NOAA) Grant NA19OAR4590341 and by NSF Grant AGS-2130936. C. Nowotarski's efforts were supported by NSF Grant AGS-1928319. J. Allen's and C. Nixon's effort was supported by NSF Grant AGS-1855054, and C. Nixon was also supported by the Earth and Ecosystem Science Ph.D. program at Central Michigan University. The National Center for Atmospheric Research is sponsored by NSF.

Data availability statement. All scripts and namelists used to generate data for this study are available at via Figshare at https://figshare.com/articles/dataset/MESO/14515560.

REFERENCES

Barnes, S. L., 1970: Some aspects of a severe, right-moving thunderstorm deduced from mesonetwork rawinsonde observations. *J. Atmos. Sci.*, **27**, 634–648, https://doi.org/10.1175/1520-0469(1970)027<0634:SAOASR>2.0.CO;2.

Brooks, H. E., C. A. Doswell III, and R. Davies-Jones, 1993: Environmental helicity and the maintenance and evolution of low-level mesocyclones. *The Tornado: Its Structure, Dynamics, Prediction, and Hazards*, *Geophys. Monogr.*, Vol. 79, Amer. Geophys. Union, 97–104.

——, ——, and J. Cooper, 1994: On the environments of tornadic and nontornadic mesocyclones. *Wea. Forecasting*, **9**, 606–618, https://doi.org/10.1175/1520-0434(1994)009<0606:OTEOTA>2.0.CO;2.

Brown, M., and C. J. Nowotarski, 2019: The influence of lifting condensation level on low-level outflow and rotation in simulated supercell thunderstorms. *J. Atmos. Sci.*, **76**, 1349–1372, https://doi.org/10.1175/JAS-D-18-0216.1.

Browning, K. A., and C. R. Landry, 1963: Airflow within a tornadic storm. Preprints, *10th Weather Radar Conf.*, Washington, DC, Amer. Meteor. Soc., 116–122.

Bryan, G. H., and J. M. Fritsch, 2002: A benchmark simulation for moist nonhydrostatic numerical models. *Mon. Wea. Rev.*, **130**, 2917–2928, https://doi.org/10.1175/1520-0493(2002)130<2917:ABSFMN>2.0.CO;2.

Bunkers, M. J., B. A. Klimowski, R. L. Thompson, and M. L. Weisman, 2000: Predicting supercell motion using a new hodograph technique. *Wea. Forecasting*, **15**, 61–79, https://doi.org/10.1175/1520-0434(2000)015<0061:PSMUAN>2.0.CO;2.

Chavas, D. R., and D. T. Dawson, 2021: An idealized physical model for the severe convective storm environmental sounding. *J. Atmos. Sci.*, **78**, 653–670, https://doi.org/10.1175/JAS-D-20-0120.1.

Coffer, B. E., and M. D. Parker, 2015: Impacts of increasing low-level shear on supercells during the early evening transition. *Mon. Wea. Rev.*, **143**, 1945–1969, https://doi.org/10.1175/MWR-D-14-00328.1.

——, and ——, 2017: Simulated supercells in nontornadic and tornadic VORTEX2 environments. *Mon. Wea. Rev.*, **145**, 149–180, https://doi.org/10.1175/MWR-D-16-0226.1.

——, and P. M. Markowski, 2018: Comments on "The regulation of tornado intensity by updraft width." *J. Atmos. Sci.*, **75**, 4049–4056, https://doi.org/10.1175/JAS-D-18-0170.1.

——, and M. D. Parker, 2018: Is there a "tipping point" between simulated nontornadic and tornadic supercells in VORTEX2 environments? *Mon. Wea. Rev.*, **146**, 2667–2693, https://doi.org/10.1175/MWR-D-18-0050.1.

——, ——, J. M. L. Dahl, L. J. Wicker, and A. J. Clark, 2017: Volatility of tornadogenesis: An ensemble of simulated nontornadic and tornadic supercells in VORTEX2 environments. *Mon. Wea. Rev.*, **145**, 4605–4625, https://doi.org/10.1175/MWR-D-17-0152.1.

——, ——, R. L. Thompson, B. T. Smith, and R. E. Jewell, 2019: Using near-ground storm relative helicity in supercell tornado forecasting. *Wea. Forecasting*, **34**, 1417–1435, https://doi.org/10.1175/WAF-D-19-0115.1.

——, M. Taszarek, and M. D. Parker, 2020: Near-ground wind profiles of tornadic and nontornadic environments in the United States and Europe from ERA5 reanalyses. *Wea. Forecasting*, **35**, 2621–2638, https://doi.org/10.1175/WAF-D-20-0153.1.

Coniglio, M. C., and M. D. Parker, 2020: Insights into supercells and their environments from three decades of targeted radiosonde observations. *Mon. Wea. Rev.*, **148**, 4893–4915, https://doi.org/10.1175/MWR-D-20-0105.1.

——, and R. E. Jewell, 2022: SPC mesoscale analysis compared to field-project soundings: Implications for supercell environment studies. *Mon. Wea. Rev.*, **150**, 567–588, https://doi.org/10.1175/MWR-D-21-0222.1.

Dahl, J. M., M. D. Parker, and L. J. Wicker, 2014: Imported and storm-generated near-ground vertical vorticity in a simulated supercell. *J. Atmos. Sci.*, **71**, 3027–3051, https://doi.org/10.1175/JAS-D-13-0123.1.

Davies-Jones, R. P., 1973: The dependence of core radius on swirl ratio in a tornado simulator. *J. Atmos. Sci.*, **30**, 1427–1430, https://doi.org/10.1175/1520-0469(1973)030<1427:TDOCRO>2.0.CO;2.

——, 1984: Streamwise vorticity: The origin of updraft rotation in supercell storms. *J. Atmos. Sci.*, **41**, 2991–3006, https://doi.org/10.1175/1520-0469(1984)041<2991:SVTOOU>2.0.CO;2.

——, 2008: Can a descending rain curtain in a supercell instigate tornadogenesis barotropically? *J. Atmos. Sci.*, **65**, 2469–2497, https://doi.org/10.1175/2007JAS2516.1.

——, 2015: A review of supercell and tornado dynamics. *Atmos. Res.*, **158–159**, 274–291, https://doi.org/10.1016/j.atmosres.2014.04.007.

——, 2017: Roles of streamwise and transverse partial-vorticity components in steady inviscid isentropic supercell-like flows. *J. Atmos. Sci.*, **74**, 3021–3041, https://doi.org/10.1175/JAS-D-16-0332.1.

——, 2021: Invented forces in supercell models. *J. Atmos. Sci.*, **78**, 2927–2939, https://doi.org/10.1175/JAS-D-21-0082.1.

——, 2022: Theory of parcel vorticity evolution in supercell-like flows. *J. Atmos. Sci.*, **79**, 1253–1270, https://doi.org/10.1175/JAS-D-21-0178.1.

——, and H. Brooks, 1993: Mesocyclogenesis from a theoretical perspective. *The Tornado: Its Structure, Dynamics, Prediction, and Hazards*, *Geophys. Monogr.*, Vol. 79, Amer. Geophys. Union, 105–114, https://doi.org/10.1029/GM079p0105.

——, D. W. Burgess, and M. Foster, 1990: Test of helicity as a forecast parameter. Preprints, *16th Conf. on Severe Local Storms*, Kananaskis Provincial Park, AB, Canada, Amer. Meteor. Soc., 588–592.

Doswell, C. A., and D. Burgess, 1993: Tornadoes and tornadic storms: A review of conceptual models. *The Tornado: Its Structure, Dynamics, Prediction, and Hazards*, *Geophys. Monogr.*, Vol. 79, Amer. Geophys. Union, 151–172.

Dowell, D. C., and H. B. Bluestein, 2002: The 8 June 1995 Mclean, Texas, storm. Part II: Cyclic tornado formation, maintenance, and dissipation. *Mon. Wea. Rev.*, **130**, 2649–2670, https://doi.org/10.1175/1520-0493(2002)130<2649:TJMTSP>2.0.CO;2.

Droegemeier, K. K., S. M. Lazarus, and R. Davies-Jones, 1993: The influence of helicity on numerically simulated convective storms. *Mon. Wea. Rev.*, **121**, 2005–2029, https://doi.org/10.1175/1520-0493(1993)121<2005:TIOHON>2.0.CO;2.

Durran, D. R., and J. B. Klemp, 1983: A compressible model for the simulation of moist mountain waves. *Mon. Wea. Rev.*, **111**, 2341–2361, https://doi.org/10.1175/1520-0493(1983)111<2341:ACMFTS>2.0.CO;2.

Fischer, J., and J. M. L. Dahl, 2020: The relative importance of updraft and cold pool characteristics in supercell tornadogenesis using highly idealized simulations. *J. Atmos. Sci.*, **77**, 4089–4107, https://doi.org/10.1175/JAS-D-20-0126.1.

——, and ——, 2022: Transition of near-ground vorticity dynamics during tornadogenesis. *J. Atmos. Sci.*, **79**, 467–483, https://doi.org/10.1175/JAS-D-21-0181.1.

Flournoy, M. D., and E. N. Rasmussen, 2021: The influence of ground-relative flow and friction on near-surface storm-relative helicity. *J. Atmos. Sci.*, **78**, 2135–2142, https://doi.org/10.1175/JAS-D-20-0320.1.

Goldacker, N. A., and M. D. Parker, 2021: Low-level updraft intensification in response to environmental wind profiles. *J. Atmos. Sci.*, **78**, 2763–2781, https://doi.org/10.1175/JAS-D-20-0354.1.

Guarriello, F., C. J. Nowotarski, and C. C. Epifanio, 2018: Effects of low-level wind profile on outflow position and near-surface vertical vorticity in simulated supercell thunderstorms. *J. Atmos. Sci.*, **75**, 731–753, https://doi.org/10.1175/JAS-D-17-0174.1.

Klemp, J. B., 1987: Dynamics of tornadic thunderstorms. *Annu. Rev. Fluid Mech.*, **19**, 369–402, https://doi.org/10.1146/annurev.fl.19.010187.002101.

——, and R. B. Wilhelmson, 1978: Simulations of right- and left-moving storms produced through storm splitting. *J. Atmos. Sci.*, **35**, 1097–1110, https://doi.org/10.1175/1520-0469(1978)035<1097:SORALM>2.0.CO;2.

Lilly, D. K., 1986: The structure, energetics, and propagation of rotating convective storms. Part II: Helicity and storm stabilization. *J. Atmos. Sci.*, **43**, 126–140, https://doi.org/10.1175/1520-0469(1986)043<0126:TSEAPO>2.0.CO;2.

Marion, G. R., and R. J. Trapp, 2019: The dynamical coupling of convective updrafts, down-drafts, and cold pools in simulated supercell thunderstorms. *J. Geophys. Res. Atmos.*, **124**, 664–683, https://doi.org/10.1029/2018JD029055.

——, ——, and S. W. Nesbitt, 2019: Using overshooting top area to discriminate potential for large, intense tornadoes. *Geophys. Res. Lett.*, **46**, 12 520–12 526, https://doi.org/10.1029/2019GL084099.

Markowski, P. M., and Y. P. Richardson, 2014: The influence of environmental low-level shear and cold pools on tornadogenesis: Insights from idealized simulations. *J. Atmos. Sci.*, **71**, 243–275, https://doi.org/10.1175/JAS-D-13-0159.1.

——, and ——, 2017: Large sensitivity of near-surface vertical vorticity development to heat sink location in idealized simulations of supercell-like storms. *J. Atmos. Sci.*, **74**, 1095–1104, https://doi.org/10.1175/JAS-D-16-0372.1.

——, J. M. Straka, and E. N. Rasmussen, 2002: Direct surface thermodynamic observations within the rear-flank downdrafts of nontornadic and tornadic supercells. *Mon. Wea. Rev.*, **130**, 1692–1721, https://doi.org/10.1175/1520-0493(2002)130<1692:DSTOWT>2.0.CO;2.

——, C. Hannon, J. Frame, E. Lancaster, A. Pietrycha, R. Edwards, and R. L. Thompson, 2003: Characteristics of vertical wind profiles near supercells obtained from the Rapid Update Cycle. *Wea. Forecasting*, **18**, 1262–1272, https://doi.org/10.1175/1520-0434(2003)018<1262:COVWPN>2.0.CO;2.

McCaul, E. W., 1991: Buoyancy and shear characteristics of hurricane-tornado environments. *Mon. Wea. Rev.*, **119**, 1954–1978, https://doi.org/10.1175/1520-0493(1991)119<1954:BASCOH>2.0.CO;2.

Morrison, H., 2017: An analytic description of the structure and evolution of growing deep cumulus updrafts. *J. Atmos. Sci.*, **74**, 809–834, https://doi.org/10.1175/JAS-D-16-0234.1.

——, and J. M. Peters, 2018: Theoretical expressions for the ascent rate of moist convective thermals. *J. Atmos. Sci.*, **75**, 1699–1719, https://doi.org/10.1175/JAS-D-17-0295.1.

——, G. Thompson, and V. Tatarskii, 2009: Impact of cloud microphysics on the development of trailing stratiform precipitation in a simulated squall line: Comparison of one- and two-moment schemes. *Mon. Wea. Rev.*, **137**, 991–1007, https://doi.org/10.1175/2008MWR2556.1.

——, J. M. Peters, W. M. Hannah, A. C. Varble, and S. E. Giangrande, 2020: Thermal chains and entrainment in cumulus updrafts: Part I: Theoretical description. *J. Atmos. Sci.*, **77**, 3637–3660, https://doi.org/10.1175/JAS-D-19-0243.1.

Murdzek, S. S., P. M. Markowski, and Y. P. Richardson, 2020: Simultaneous dual-Doppler and mobile mesonet observations of streamwise vorticity currents in three supercells. *Mon. Wea. Rev.*, **148**, 4859–4874, https://doi.org/10.1175/MWR-D-20-0239.1.

Naylor, J., and M. S. Gilmore, 2012: Convective initiation in an idealized cloud model using an updraft nudging technique. *Mon. Wea. Rev.*, **140**, 3699–3705, https://doi.org/10.1175/MWR-D-12-00163.1.

Nowotarski, C. J., and A. A. Jensen, 2013: Classifying proximity soundings with self-organizing maps toward improving supercell and tornado forecasting. *Wea. Forecasting*, **28**, 783–801, https://doi.org/10.1175/WAF-D-12-00125.1.

Orf, L., R. Wilhelmson, B. Lee, C. Finley, and A. Houston, 2017: Evolution of a long-track violent tornado within a simulated supercell. *Bull. Amer. Meteor. Soc.*, **98**, 45–68, https://doi.org/10.1175/BAMS-D-15-00073.1.

Parker, M. D., 2014: Composite VORTEX2 supercell environments from near-storm soundings. *Mon. Wea. Rev.*, **142**, 508–529, https://doi.org/10.1175/MWR-D-13-00167.1.

——, and J. M. L. Dahl, 2015: Production of near-surface vertical vorticity by idealized downdrafts. *Mon. Wea. Rev.*, **143**, 2795–2816, https://doi.org/10.1175/MWR-D-14-00310.1.

Peters, J. M., C. Nowotarski, and H. Morrison, 2019: The role of vertical wind shear in modulating maximum supercell updraft velocities. *J. Atmos. Sci.*, **76**, 3169–3189, https://doi.org/10.1175/JAS-D-19-0096.1.

——, H. Morrison, W. M. Hannah, A. C. Varble, and S. E. Giangrande, 2020a: Thermal chains and entrainment in cumulus updrafts: Part II: Simulations. *J. Atmos. Sci.*, **77**, 3661–3681, https://doi.org/10.1175/JAS-D-19-0244.1.

——, ——, C. J. Nowotarski, J. P. Mulholland, and R. L. Thompson, 2020b: A formula for the maximum vertical velocity in supercell updrafts. *J. Atmos. Sci.*, **77**, 3747–3757, https://doi.org/10.1175/JAS-D-20-0103.1.

——, C. J. Nowotarski, and G. Mullendore, 2020c: Are supercells resistant to entrainment because of their rotation? *J. Atmos. Sci.*, **77**, 1475–1495, https://doi.org/10.1175/JAS-D-19-0316.1.

——, ——, and J. P. Mulholland, 2020d: The influences of effective inflow layer streamwise vorticity and storm-relative flow on supercell updraft properties. *J. Atmos. Sci.*, **77**, 3033–3057, https://doi.org/10.1175/JAS-D-19-0355.1.

——, H. Morrison, T. C. Nelson, J. N. Marquis, J. P. Mulholland, and C. J. Nowotarski, 2022a: The influence of shear on deep convection initiation. Part I: Theory. *J. Atmos. Sci.*, **79**, 1669–1690, https://doi.org/10.1175/JAS-D-21-0145.1.

——, ——, ——, ——, ——, and ——, 2022b: The influence of shear on deep convection initiation. Part II: Simulations. *J. Atmos. Sci.*, **79**, 1691–1711, https://doi.org/10.1175/JAS-D-21-0144.1.

——, J. P. Mulholland, and D. R. Chavas, 2022c: Generalized lapse rate formulas for use in entraining cape calculations. *J. Atmos. Sci.*, **79**, 815–836, https://doi.org/10.1175/JAS-D-21-0118.1.

Rotunno, R., and J. B. Klemp, 1985: On the rotation and propagation of simulated supercell thunderstorms. *J. Atmos. Sci.*, **42**, 271–292, https://doi.org/10.1175/1520-0469(1985)042<0271:OTRAPO>2.0.CO;2.

Schueth, A., C. Weiss, and J. M. L. Dahl, 2021: Comparing observations and simulations of the streamwise vorticity current and the forward-flank convergence boundary in a supercell storm. *Mon. Wea. Rev.*, **149**, 1651–1671, https://doi.org/10.1175/MWR-D-20-0251.1.

Sessa, M. F., and R. J. Trapp, 2020: Observed relationship between tornado intensity and pretornadic mesocyclone characteristics. *Wea. Forecasting*, **35**, 1243–1261, https://doi.org/10.1175/WAF-D-19-0099.1.

Skinner, P. S., C. C. Weiss, M. M. French, H. B. Bluestein, P. M. Markowski, and Y. P. Richardson, 2014: VORTEX2 observations of a low-level mesocyclone with multiple internal rear-flank downdraft momentum surges in the 18 May 2010 Dumas, Texas, Supercell. *Mon. Wea. Rev.*, **142**, 2935–2960, https://doi.org/10.1175/MWR-D-13-00240.1.

Smith, B. T., R. L. Thompson, J. S. Grams, C. Broyles, and H. E. Brooks, 2012: Convective modes for significant severe thunderstorms in the contiguous United States. Part I: Storm classification and climatology. *Wea. Forecasting*, **27**, 1114–1135, https://doi.org/10.1175/WAF-D-11-00115.1.

Taszarek, M., J. T. Allen, T. Púcik, K. A. Hoogewind, and H. E. Brooks, 2020: Severe convective storms across Europe and the United States. Part II: ERA5 environments associated with lightning, large hail, severe wind, and tornadoes. *J. Climate*, **33**, 10 263–10 286, https://doi.org/10.1175/JCLI-D-20-0346.1.

Thompson, R. L., 1998: Eta model storm-relative winds associated with tornadic and nontornadic supercells. *Wea. Forecasting*, **13**, 125–137, https://doi.org/10.1175/1520-0434(1998)013<0125:EMSRWA>2.0.CO;2.

——, R. Edwards, J. A. Hart, K. L. Elmore, and P. Markowski, 2003: Close proximity soundings within supercell environments obtained from the Rapid Update Cycle. *Wea. Forecasting*, **18**, 1243–1261, https://doi.org/10.1175/1520-0434(2003)018<1243:CPSWSE>2.0.CO;2.

——, C. M. Mead, and R. Edwards, 2007: Effective storm-relative helicity and bulk shear in supercell thunderstorm environments. *Wea. Forecasting*, **22**, 102–115, https://doi.org/10.1175/WAF969.1.

——, B. T. Smith, J. S. Grams, A. R. Dean, and C. Broyles, 2012: Convective modes for significant severe thunderstorms in the contiguous United States. Part II: Supercell and QLCS tornado environments. *Wea. Forecasting*, **27**, 1136–1154, https://doi.org/10.1175/WAF-D-11-00116.1.

Trapp, R. J., G. R. Marion, and S. W. Nesbitt, 2017: The regulation of tornado intensity by updraft width. *J. Atmos. Sci.*, **74**, 4199–4211, https://doi.org/10.1175/JAS-D-16-0331.1.

——, ——, and ——, 2018: Reply to "Comments on 'The regulation of tornado intensity by updraft width.'" *J. Atmos. Sci.*, **75**, 4057–4061, https://doi.org/10.1175/JAS-D-18-0276.1.

Warren, R. A., H. Richter, H. A. Ramsay, S. T. Siems, and M. J. Manton, 2017: Impact of variations in upper-level shear on simulated supercells. *Mon. Wea. Rev.*, **145**, 2659–2681, https://doi.org/10.1175/MWR-D-16-0412.1.

Wicker, L. J., and R. B. Wilhelmson, 1995: Simulation and analysis of tornado development and decay within a three-dimensional supercell thunderstorm. *J. Atmos. Sci.*, **52**, 2675–2703, https://doi.org/10.1175/1520-0469(1995)052<2675:SAAOTD>2.0.CO;2.

Wurman, J., D. Dowell, Y. Richardson, P. Markowski, E. Rasmussen, D. Burgess, L. Wicker, and H. B. Bluestein, 2012: The second Verification of the Origins of Rotation in Tornadoes Experiment: VORTEX2. *Bull. Amer. Meteor. Soc.*, **93**, 1147–1170, https://doi.org/10.1175/BAMS-D-11-00010.1.